A&A 508, 805–821 (2009)
DOI: 10.1051/0004-6361/20077981

Astronomy & Astrophysics

Phase-resolved *XMM-Newton* observations of the massive WR+O binary WR 22⋆

E. Gosset[1,⋆⋆], Y. Nazé[1,⋆⋆⋆], H. Sana[2], G. Rauw[1,⋆⋆], and J.-M. Vreux[1]

[1] Institut d'Astrophysique et de Géophysique, Université de Liège, allée du six août 17, Bat.B5c, 4000 Liège, Belgium
e-mail: gosset@astro.ulg.ac.be
[2] European Southern Observatory, Alonso de Cordova 3107, Vitacura, Casilla 19001, 19 Santiago de Chile, Chile

Received 31 May 2007 / Accepted 25 May 2009

ABSTRACT

Aims. To better understand the phenomenon of colliding winds in massive binary stars, we study the X-ray lightcurve of a WR+O system of the Carina region, a system well known for the high mass of its primary.
Methods. Phase-resolved X-ray observations of the massive WR+O binary system WR 22 were performed with the *XMM-Newton* facility. We observed the object at seven different phases from near apastron to near periastron.
Results. The X-ray spectrum can be represented by a two-component, optically thin, thermal plasma model with a first one at a typical temperature of 0.6 keV and a second hotter one in the range 2.0–4.5 keV. The hot component is indicative of a colliding wind phenomenon, but its flux is remarkably constant with time despite the high eccentricity of the orbit. Although surprising at first, this actually does not contradict the results of the hydrodynamical simulations of the wind collision that we performed. When the system goes from apastron to periastron, the soft part of the X-ray flux is progressively lowered by an increasing intervening absorbing column. This behaviour can be interpreted in terms of an X-ray emitting plasma located near the O star, but not fully intrinsic to it, and accompanying the star when it dives into the wind of the WR component. A model is presented that interprets most of the observational constraints. This model suggests that the mass-loss rate of $\dot{M}_{\rm WR} \sim 1.6 \times 10^{-5}\,M_{\odot}\,{\rm yr}^{-1}$ assumed for the WR could still be slightly too high, whereas it is already lower than other published values. From the comparison of the observed and the expected absorptions at phases near periastron, we deduce that the hard X-ray emitting collision zone should at least have a typical size of 50–60 $R_{\odot}$, but that the size for the soft X-ray emitting region could reach 244 $R_{\odot}$ if the assumed mass-loss rate is correct. We also present an upper limit to the X-ray luminosity of the WR component that further questions the existence of intrinsic X-ray emission from single WN stars.

Key words. stars: Wolf-Rayet – stars: individual: WR 22 – binaries: general – X-rays: stars – X-rays: binaries

1. Introduction

Thirty years ago, the *EINSTEIN* satellite serendipitously discovered that early-type stars are moderate X-ray emitters (Harnden et al. 1979; Seward et al. 1979). Several subsequent studies progressively converged to indicate that the observed X-ray luminosity of single OB stars is proportional to their bolometric luminosity with $L_{\rm X}/L_{\rm bol} \sim 10^{-7}$ (Pallavicini et al. 1981; Seward & Chlebowski 1982; Berghöfer et al. 1997; Sana et al. 2006).

Among the first early-type stars detected by *EINSTEIN* in the Carina region, two WR stars were already present (WR 25, Seward et al. 1979; and WR 22, Seward & Chlebowski 1982). Although some WR stars seem to be intrinsic X-ray emitters (see e.g. the *ROSAT* results by Pollock et al. 1995), the actual situation is less clear than for the O type stars. Wessolowski (1996) found no obvious relation between the X-ray luminosity of WR stars and other physical parameters of these stars (bolometric luminosity, wind momentum, etc.). These results and more recent ones suggest that not detect some WR stars could stem from the high opacity of their wind that prevents most of the X-ray photons from escaping (Ignace & Oskinova 1999; Oskinova et al. 2003; Gosset et al. 2005).

The situation is quite different for double systems. Pollock (1987) and Chlebowski & Garmany (1991) noticed that massive binaries were characterised by higher X-ray luminosities than expected from the mere sum of the intrinsic emissions from the two individual stars. It became evident that the strong and fast winds of the two star components were bound to violently collide, producing a very hot plasma and thus a third source of X-ray emission (see e.g. Cherepashchuk 1976; Prilutskii & Usov 1976; or Stevens et al. 1992, and references therein).

These colliding wind systems often exhibit an X-ray modulation with the binary cycle either because of the eccentricity and the related change of distance between the two stars or because of the varying circumstellar opacity along the line of sight to the collision zone, resulting from the particular orientation of the system with respect to the observer. However, serious investigations of these variations required high-quality facilities that have only been launched recently. Several O+O binaries have been observed with *XMM-Newton*, revealing different kinds of phase-locked modulations (e.g. HD 152248; Sana et al. 2004, HD 93403; Rauw et al. 2002, HD 159176; De Becker et al. 2004, for a review see Rauw 2006).

Little has been done up to now about classical WR+O binary systems. Willis et al. (1995) reports a detailed *ROSAT* study

⋆ Based on observations with *XMM-Newton*, an ESA Science Mission with instruments and contributions directly funded by ESA Member States and the USA (NASA).
⋆⋆ Research Associate FNRS (Belgium).
⋆⋆⋆ Postdoctoral Researcher FNRS (Belgium).

Table 1. Main orbital elements of WR 22 from the two most recent solutions.

	Rauw et al. (1996)		Schweickhardt et al. (1999)	
Parameter	Value	Std Deviation	Value	Std Deviation
P (days)	80.325	0.010	80.336	0.0013
e	0.559	0.013	0.598	0.010
γ_{WR} (km s^{-1})	–29.8	1.0	0(adopted)	15.
γ_O (km s^{-1})	+21.3	10.4	0(adopted)	15.
K_{WR} (km s^{-1})	72.3	1.48	70.6	0.8
K_O (km s^{-1})	201.4	14.8	190.0	10.0
ω (degree)	271.6	2.8	268.2	1.6
T_0 (HJD 2400000+)[1]	49324.17	0.30	50127.47	0.14
$a_{WR} \sin i$ (10^6 km)	66.3	1.5	62.5	0.9
$a_O \sin i$ (10^6 km)	185.0	14.8	168.2	9.0
$q = M_{WR}/M_O$	2.78	0.21	2.69	0.14
$M_{WR} \sin^3 i$ ($M_\odot$)	71.7	11.0	55.3	7.3
$M_O \sin^3 i$ ($M_\odot$)	25.7	2.3	20.6	1.7
$T_{eclipse}$ (HJD 2400000+)	49324.09	0.30	50127.55	0.14

[1] The time of periastron passage.

of γ^2 Vel (WC8+O9I, P = 78.9 d). They detected an orbital phase-locked systematic variation. The observed X-ray emission strongly increases when the O companion, with its less opaque wind, is in front of the WC star. At this particular phase, the line of sight to the observer essentially goes through the O wind and unveils the X-ray emitting wind interaction zone that is much more absorbed at other phases due to the intervening dense WR wind. This result has been confirmed and further refined by more recent observations and models (Schild et al. 2004; Henley et al. 2005).

Similar behaviour is observed for the very eccentric long-period binary system WR 140 (WC7+O4-5, P = 8 yr; Zhekov & Skinner 2000; Pollock et al. 2005; and references therein). Near periastron, the flux rises quickly as the stellar separation decreases, but as the WR moves in front of the O component, the opacity of the WR wind is decisive.

Our knowledge and understanding of colliding wind binaries (CWB) and of their X-ray emission is still in its infancy. It should be pointed out that only a handful of binary systems have been investigated. More effort is needed to tie in models with observations. From the observational point of view, it is necessary to increase the number of studied systems to improve the variety of objects and to broaden the space of covered parameters. In this framework, we decided to study WR 22 with *XMM-Newton*. WR 22 is a very massive WR+O binary with a primary of spectral type WN7+abs and characterised by a mass of at least 56 $M_\odot$. This object is probably a massive star still in the core-hydrogen burning phase but in WR clothing. The O component is a mid to late O-type star. Both stars should have strong winds. Therefore, WR 22 is a good candidate for an extreme case of CWB.

We obtained seven *XMM-Newton* pointings at WR 22 covering the orbit from apastron to periastron, and the results of this campaign are the subject of the present paper. Section 2 summarises the characteristics of the WR 22 system. Section 3 describes the observations and their reduction. A detailed study of the data is to be found in Sect. 4, whereas Sect. 5 contains a first tentative modelling of the observations and discussions. Section 6 offers a summary of the results.

2. The massive binary WR 22

WR 22 is a Wolf-Rayet (WR) star member of the Carina OB1 association (Lundström & Stenholm 1984). The spectrum of the star exhibits a large amount of hydrogen ($X_H \sim 40\%$, Hamann et al. 1991; $X_H \sim 44\%$, Crowther et al. 1995a). Since the work of Niemela (1973), it has also been known as a WR star that exhibits radial velocity variations, as well as absorption components in the upper Balmer lines. WR 22 was therefore classified SB1 (van der Hucht et al. 1981) and was given a spectral type WN7+abs. Other works by Moffat & Seggewiss (1978) and Conti et al. (1979) attributed to the system an orbital period of 80.35 days and an eccentricity around 0.55. However, the Balmer line-absorption components were found to follow the WR movement. Therefore, no trace of the companion was detected, except perhaps for very weak auxiliary absorption components suspected on a few spectrograms (Conti et al. 1979; but mainly Niemela 1979). However, it finally became clear that the companion should be detectable with the discovery (Balona et al. 1989; Gosset et al. 1991) that WR 22 exhibits an eclipse corresponding to the WR being in front of its companion. Only one eclipse occurs: the secondary one.

After a spectroscopic campaign spanning several years, Rauw et al. (1996) were the first to be able to trace the full orbit of the companion. This work was based on numerous high signal-to-noise ratio spectra, acquired between 1986 and 1992, allowing the weak lines of the secondary that are of the order of 1–2% of the continuum to be spotted. Rauw et al. (1996) derived the first SB2 orbital solution. The parameters are reproduced in Table 1: the minimum masses amounted to 71.7 and 25.7 $M_\odot$, making the WR 22 primary one of the heaviest (the heaviest at that time) WR stars ever weighed. The error bars for the minimum masses, underestimated in that paper, are corrected in Table 1. Such a high mass, not to mention the observed hydrogen content, was suggesting that the WR component of WR 22 only recently entered into the WR stage or even that it could be a very luminous core-hydrogen burning star disguised into a WR (Rauw et al. 1995). Because the companion is 2.3 mag fainter than the WR in the continuum, Rauw et al. (1996) suggest that it is a main sequence star and report a tentative spectral type of O7.5V (O6.5V–O8.5V).

Later, the orbital solution was reestimated by Schweickhardt et al. (1999) on the basis of a new observational campaign spanning 104 contiguous days and consisting of 88 spectra. The relevant parameters are also given in Table 1. Schweickhardt et al. (1999) suggest a spectral type O9III-V (O8–O9.5) for the companion. The solution of Schweickhardt et al. (1999) led to a significant revision of the mass of the WR down to a minimum

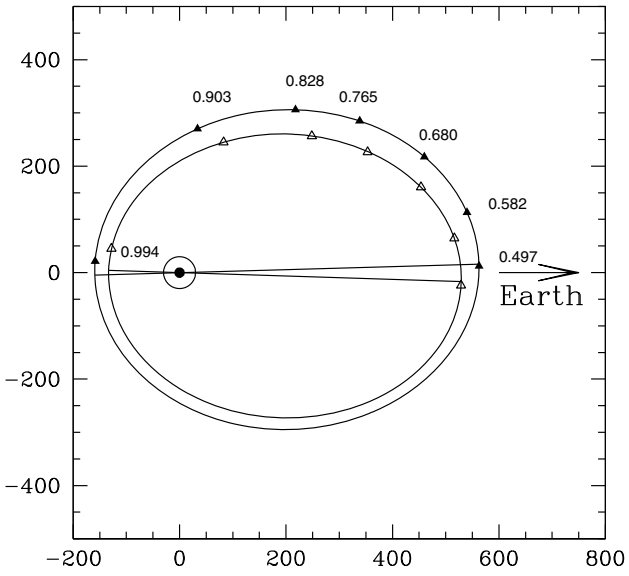

Fig. 1. Projection on a plane defined by the line of sight to the observer and the line of nodes of the orbit of the O companion around the WR component in WR 22. The image is made in the rest frame of the WR star (coordinates 0., 0.), and the two orbital solutions suggested in the literature are considered. The position of the O star as a function of the phases corresponding to the *XMM-Newton* observations are indicated by triangles (filled: Rauw et al. 1996; open: Schweickhardt et al. 1999). The dimensions are expressed in solar radii on both axes and the adopted orbital inclination is 85°.

mass of 55.3 $M_\odot$. Besides a slight shift of the period, the two consequent discrepancies between the two solutions concern the eccentricity going from $e = 0.559 \pm 0.013$ to $e = 0.598 \pm 0.010$ and the radial velocity semi-amplitude of the O star going from $K_O = 201.4 \pm 14.8$ to $K_O = 190.0 \pm 10.0$. Part of the discrepancy could of course be due to a different treatment of the systemic velocities. It is worth noting that, contrary to the Rauw et al. case, the individual He I lines of the companion are not visible in the spectra acquired by Schweickhardt et al. (1999): they instead had to construct a mean dynamical spectrum to derive the orbit of the companion. However, there are more acquired spectra than for the Rauw et al. (1996) solution. In any case, both values of the WR minimum mass are in the error bars of each other, and both solutions appear equally relevant. With the available data, it is extremely difficult to make a decision about the true orbital solution. Both of them are illustrated in Fig. 1, and we briefly come back to this point in Sect. 5. It is interesting to note that the eclipse roughly covers the phase interval from $\phi = 0.987$ to 1.011 and is centred on $\phi = 0.999$. From the study of the eclipses, an inclination angle in the range 78°–88° is deduced, as well as a rather modest mass-loss rate (value assumed: $1.6 \times 10^{-5}\ M_\odot\ \mathrm{yr}^{-1}$, see Rauw 1997).

In the present paper, we adopt the visual magnitude $V \sim v = 6.42$ for WR 22 (Johnson et al. 1966; Smith 1968; in the Westerlund-Smith narrow-band system) and a colour excess $E_{B-V} = 0.36$. Assuming a distance of 2.7 kpc, we adopt the distance modulus DM = 12.15. The calculated extinction amounts to $A_V = 3.1 \times 0.36 = 1.12$ leading to an absolute magnitude for the system of $M_v^{\mathrm{WR+O}} = -6.85$, in good agreement with the value adopted by Crowther et al. (1995b). When we trust the continuum luminosity ratio of 8.2 derived by Rauw et al. (1996), we deduce absolute magnitudes $M_v^{\mathrm{WR}} = -6.73$ and $M_v^{\mathrm{O}} = -4.44$ to be compared with the values in the case of total eclipse of the O star (extreme case) given by $M_v^{\mathrm{WR}} = -6.77$ and $M_v^{\mathrm{O}} = -4.02$ (Schweickhardt et al. 1999). Compared to the absolute-magnitude scale of the calibration of Howarth & Prinja (1989), $M_v^{\mathrm{O}} = -4.44$ is consistent with an O7-9V star. The giant luminosity class is rejected, provided that our adopted estimate for the distance (2.7 kpc) is roughly correct. Indeed, a large distance of 3.65 kpc would be requested for the O star to be bright enough for a possible classification as a giant (i.e. at least $M_v^{\mathrm{O}} = -5.1$). This would imply an unrealistically high $M_v^{\mathrm{WR}} = -7.39$ which we consider, along with the necessary distance, unlikely.

3. Observations and data reduction

The massive binary WR 22 was observed with the *XMM-Newton* observatory (Jansen et al. 2001) on seven occasions distributed over two groups (programme 010947). The first round took place in July-August 2001, whereas the second one occurred in December 2001–January 2002. All the pointings were accurately centred on WR 22 and had nominal exposure times of 10 ks. A detailed journal of these observations is available in Table 2: Col. 1 gives an internal numbering of the pointings, while Col. 2 gives the orbit number and Col. 3 the observation ID. The date corresponding to the mid-exposure, the heliocentric Julian date (HJD) and the phase of the binary system are shown in Cols. 4 to 6. Phase zero corresponds to periastron. These phases are computed according to the ephemerides of Rauw et al. (1996, see Table 1). The phases computed using the ephemerides of Schweickhardt et al. (1999) are actually smaller by 0.004. The observation duration can be found in Col. 7 while Cols. 8 to 10 represent the effective exposure time after discarding soft proton-flare periods (see below). The position angle of the satellite is provided in the last column.

The two EPIC-MOS instruments (Turner et al. 2001), as well as the EPIC-pn detector (Strüder et al. 2001), were operated in the full frame mode. To reject UV/optical light from the bright main target, the three EPIC instruments were used with the thick filter. Because of the brightness of WR 22 in the visible domain, the OM instrument (Mason et al. 2001) was switched off, whereas the star is too faint in the X-ray domain to lead to useful RGS spectra (den Herder et al. 2001).

We used version 5.3.3 of the *XMM-Newton* Science Analysis Software (SAS) to reduce the raw EPIC data. We applied the *emproc* and *epproc* pipeline procedures to the EPIC-MOS and the EPIC-pn raw data, respectively, taking particular care to ensure a proper treatment of the gaps and bad columns. We restricted the useful MOS events to those with a pattern in the range 0 to 12 and complying with the selection criterion XMMEA_EM. For the pn detector, we restricted ourselves to one and two photon events (pattern 0–4) and to a flag of zero. No pile-up is present in the data. We further filtered the event lists to remove the epochs affected by soft proton flares. Pointing I was affected by a marked soft proton flare that took place a few ks after the beginning of the exposure. It evolved into such a strong flare that the exposure was prematurely ended by the operator. Only 20% of the foreseen duration was saved. For the pn detector, the exposure started later (just at the beginning of the flare) can be considered useless. The pointings II, III, and VI were entirely free of soft proton flares, but the background, although constant, is slightly stronger for pointing VI. On the opposite, the end of pointing V was affected by soft protons and we restricted the exposure to its first part amounting to some 7.5 ks only (48%) for the MOS detectors. Pointings IV and VII present various small flares that were filtered out. The resulting effective exposure times are given in Table 2.

Table 2. Journal of the X-ray observations of WR 22.

No.	Orbit	Obs. ID	Date (yyyy-mm-dd)	HJD (2450000+)	Phase	Observ. Duration (s)	Effective exposure (s) MOS1	(s) MOS2	(s) pn	Pos. Angle (ddd:am:as.s)
I	287	0109470101	2001-07-04	2095.15202	0.497	13239	2568	2571	0	307:19:30.7
II	291	0109470201	2001-07-11	2101.99880	0.582	13254	12392	12394	9066	315:32:04.5
III	301	0109470301	2001-07-31	2121.76809	0.828	13239	12316	12323	8986	332:01:21.2
IV	304	0109470501	2001-08-06	2127.74921	0.903	13335	10205	10514	6459	337:06:12.6
V	307	0109470601	2001-08-13	2135.04586	0.994	16039	7523	7520	4792	000:42:34.5
VI	375	0109470701	2001-12-27	2270.52715	0.680	13319	12156	12151	8611	120:52:46.3
VII	379	0109471001	2002-01-02	2277.36437	0.765	16033	14223	13940	8954	129:44:49.6

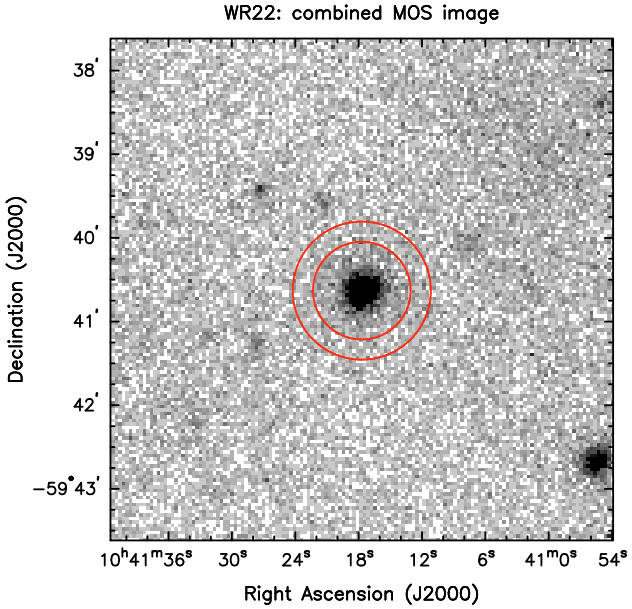

Fig. 2. Combined (pointings II to VII) MOS1+MOS2 X-ray image of WR 22 in the [0.5–10 keV] band. The positions of the events were binned, and we adopted a pixel size of 2.″5. The extraction regions for the source and the background are delimited by concentric circles of radii 35″ and 49.″5.

On the basis of the cleaned event lists, we built images of the field in various bands as well as in the total band [0.5–10 keV], for each of the three instruments and for each pointing. We also built images combining either two MOS instruments, or the two MOS and the pn instruments on the basis of the merging of the relevant event lists. We also combined lists from different pointings. Figure 2 is one of these images depicting the field of WR 22.

The count rates of the central source, WR 22, were computed by first integrating the counts inside a circle with a 35″ radius. The background is estimated in a surrounding annulus reaching 49.″5 and designed such that this region has the same area as the inner circle (see Fig. 2). As a check, we also extracted the background at different places on the same CCD. No anomaly was detected and the annulus value was always adopted. Concerning the pn detector, we extracted the background in nearby ad hoc circles positioned on the same CCD and cautiously avoiding the other sources in the field. The background-corrected counts were divided by the average exposure time over the central circle to obtain count rates. The count rates are given in Table 3, and were not corrected for the portion of the point spread function (psf) that is outside the circle. The proportion of photons inside the extraction region is around 84% and the correction factor is thus 1.19. We extracted X-ray lightcurves for WR 22 within each pointing. WR 22 does not show any variability during the different pointings beyond the Poissonian fluctuations (see also Claeskens et al. 2009). For each pointing and for each instrument, we also extracted the corresponding X-ray spectra of WR 22.

Table 3. Observed count rates associated with WR 22 in the different energy bands: total [0.5–10. keV], soft [0.5–1.0 keV], medium [1.0–2.0 keV], hard [2.0–10. keV].

Phase	No.	Band	MOS1 cts/s	MOS2 cts/s	pn cts/s
0.497	I	Total	0.0300 (46)	0.0334 (45)	–
0.497	I	Soft	0.0074 (26)	0.0109 (26)	–
0.497	I	Med.	0.0148 (30)	0.0159 (29)	–
0.497	I	Hard	0.0078 (23)	0.0066 (22)	–
0.582	II	Total	0.0401 (21)	0.0399 (21)	0.1357 (44)
0.582	II	Soft	0.0156 (13)	0.0152 (14)	0.0673 (32)
0.582	II	Med.	0.0178 (14)	0.0190 (14)	0.0533 (26)
0.582	II	Hard	0.0067 (09)	0.0061 (08)	0.0150 (16)
0.680	VI	Total	0.0384 (21)	0.0397 (22)	0.1458 (48)
0.680	VI	Soft	0.0151 (14)	0.0172 (15)	0.0706 (34)
0.680	VI	Med.	0.0174 (13)	0.0173 (14)	0.0591 (28)
0.680	VI	Hard	0.0058 (09)	0.0053 (09)	0.0161 (19)
0.765	VII	Total	0.0317 (18)	0.0313 (18)	0.1004 (41)
0.765	VII	Soft	0.0114 (12)	0.0102 (12)	0.0447 (28)
0.765	VII	Med.	0.0137 (11)	0.0157 (12)	0.0408 (23)
0.765	VII	Hard	0.0066 (08)	0.0055 (08)	0.0149 (17)
0.828	III	Total	0.0286 (19)	0.0325 (20)	0.1052 (41)
0.828	III	Soft	0.0066 (11)	0.0088 (12)	0.0347 (27)
0.828	III	Med.	0.0167 (14)	0.0173 (13)	0.0527 (26)
0.828	III	Hard	0.0052 (08)	0.0063 (08)	0.0178 (17)
0.903	IV	Total	0.0253 (19)	0.0232 (19)	0.0794 (44)
0.903	IV	Soft	0.0046 (10)	0.0048 (12)	0.0204 (28)
0.903	IV	Med.	0.0144 (14)	0.0126 (13)	0.0425 (28)
0.903	IV	Hard	0.0063 (09)	0.0059 (08)	0.0166 (20)
0.994	V	Total	0.0166 (21)	0.0168 (20)	0.0410 (44)
0.994	V	Soft	0.0025 (11)	0.0035 (11)	0.0074 (28)
0.994	V	Med.	0.0077 (14)	0.0080 (13)	0.0225 (25)
0.994	V	Hard	0.0064 (11)	0.0053 (10)	0.0111 (22)

4. Observational results

4.1. The count rates

We computed the count rates of the central source in four energy ranges: a total [0.5–10. keV], a soft [0.5–1.0 keV], a medium [1.0–2.0 keV], and a hard [2.0–10. keV] bandpass. The results

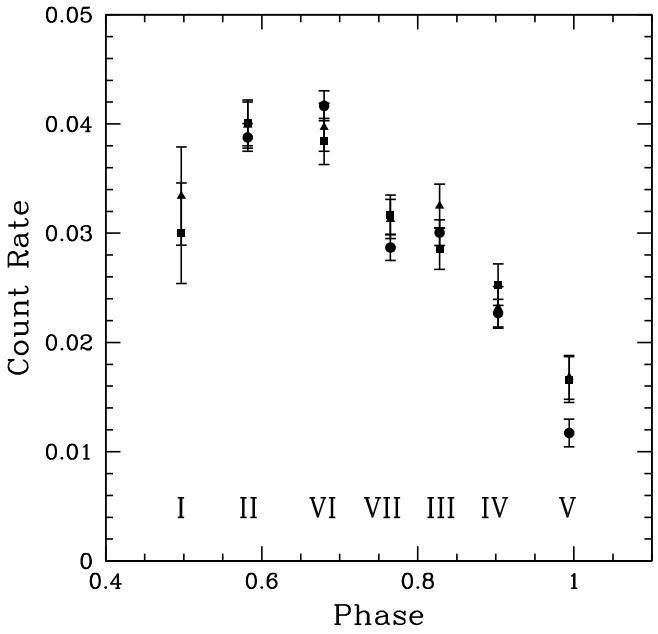

Fig. 3. Evolution of the observed count rates in the [0.5, 10 keV] band as a function of the orbital phase (Table 3). Periastron is at phase 1.0, whereas apastron is at phase 0.5. The triangles represent the MOS1 detections, whereas the squares designate the MOS2 ones. Circles represent the pn detector count rates arbitrarily divided by 3.5 to ease the comparison with the other two detectors. Error bars represent ±1 standard deviation.

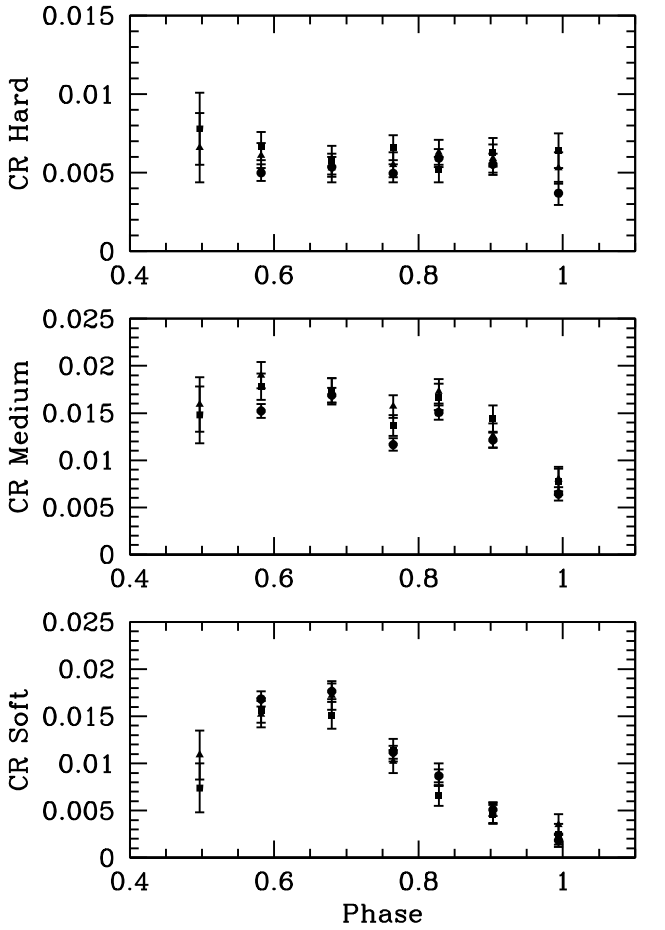

Fig. 4. Evolution of the observed count rates in the three bands, soft [0.5, 1.0 keV], medium [1.0, 2.0 keV], and hard [2.0, 10. keV], as a function of the orbital phase (Table 3). The observed count rates are given for both MOS detectors (MOS1: triangles; MOS2: squares), whereas those of the pn detector (circles) are divided by 4.0, 3.5, and 3.0, for the soft, the medium, and the hard bands, respectively. Error bars represent ±1 standard deviation.

are given in Table 3. The reported counts correspond to the extraction region and are not corrected for the extension of the psf beyond the circle. The figures in parentheses indicate one standard deviation. They are expressed in units of the least significant digits of the given value. Figure 3 shows the evolution of the observed count rates in the total band for each instrument as a function of the orbital phase of the system. The count rates systematically decrease when going from orbital phase 0.58 (right after apastron) to periastron. The effect seems to be phase-locked and, despite the data not all being acquired during the same orbital cycle, the lightcurve is rather smooth, pointing to a strong stability of the mechanism producing the intensity variations. As mentioned before, the pointing near apastron (I) is characterised by a large error, and the actual value of the count rates at that phase is highly uncertain. The only constraint that can be obtained on the count rate at apastron is the upper limit (Poissonian equivalent to a 3σ deviation) on the observed value: it cannot be 25% higher than the values at pointings II ($\phi = 0.582$) and VI ($\phi = 0.680$).

To further investigate the variability, we plotted the extracted count rates for the individual energy bands in Fig. 4. The variability is clear and well-marked in the soft band [0.5–1.0 keV], and the count rate at the pointing nearest to periastron only amounts to 13–16% of its value near apastron (pointings II and VI). The variability is less marked in the medium band. Although the flux is low in the hard energy band, we can nevertheless conclude that it is rather constant over the cycle. To further analyse this behaviour, we now study the X-ray spectrum in more detail.

4.2. The X-ray spectrum

Figure 5 illustrates the variation in the X-ray spectrum of WR 22 while the binary star is moving from near apastron to near periastron. It is immediately clear that the soft part of the spectrum gradually decreases in intensity, whereas the hard part is rather constant. The loss of intensity is progressive with phase and increases when going to lower photon energy. The easiest way to explain this X-ray lightcurve and the behaviour of the spectra, is by invoking a rather constant X-ray emission (in all energy bands) absorbed by an increasingly large column when going from about apastron to periastron. Because of the eccentricity of the orbit when going to periastron, the O star progressively dives into the WR wind. It is thus tempting to imagine that the X-ray emitting plasma, or part of it, is broadly following a motion similar to the O companion.

Emission lines are clearly visible in the X-ray spectra (Fig. 5). Table 4 presents a list of identified lines. The responsible ion and the energy of the transition are given in the first two columns. The third column contains the type of the transition. The fourth and fifth ones mention the temperatures corresponding to the maximum intensity of the line (Mewe et al. 1985): they are expressed in log-temperature (in K) and in equivalent energy (in keV). The emission lines are considered further in Sect. 4.2.1.

The Mg XI line is clearly present and corresponds to a thermal plasma temperature of the order of 6 MK (see Mewe et al. 1985). The line of Si XIII instead suggests a temperature of

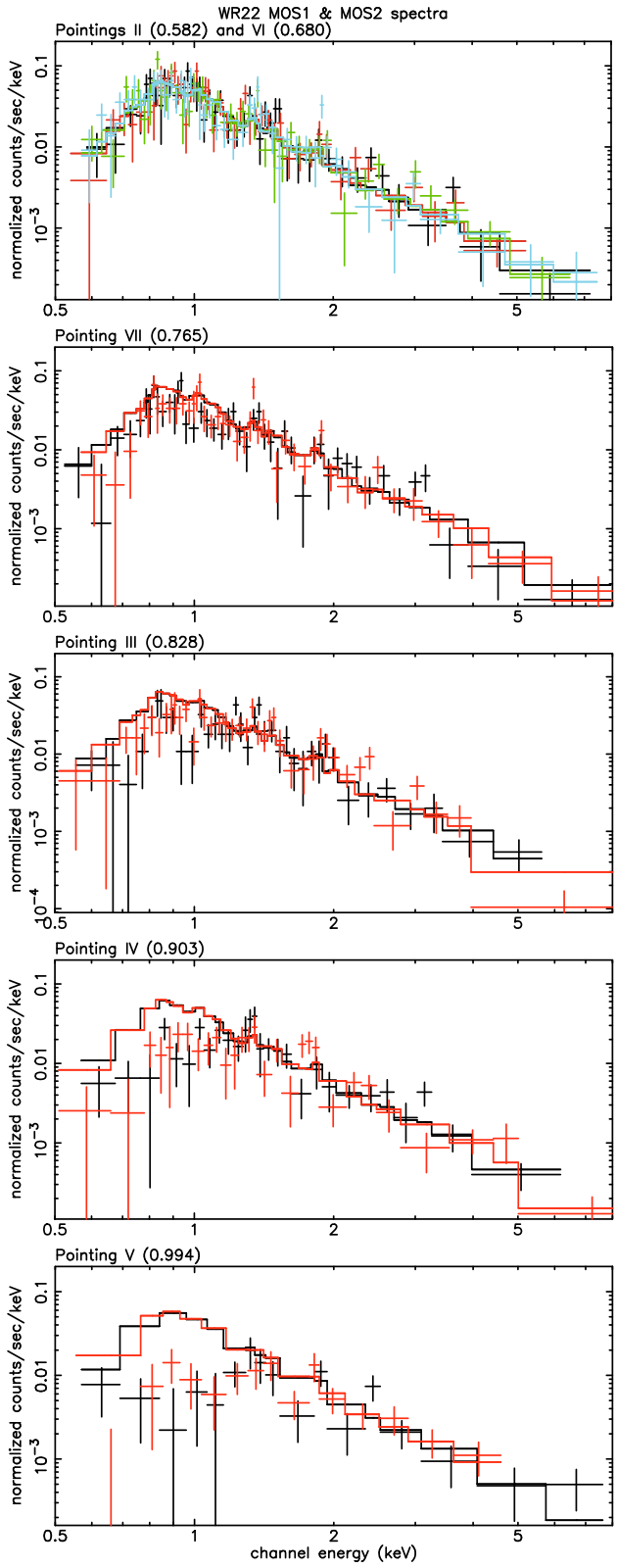

Fig. 5. Evolution of the X-ray spectrum (MOS) of WR 22 as a function of the phase. The data with error bars (Poissonian $\pm 1\sigma$ deviation) represent the observations, whereas the broken continuous lines represent the model (MOS1 is in black, MOS2 in red). The pointing identification and the relevant phase are given at the top left of each panel. *In the upper panel*, the pointings II and VI are shown together (green and blue for MOS1 and MOS2 of pointing VI). The model shown in each panel is the 2-T `mekal` model as fitted simultaneously to the pointings II and VI (illustrated in *the upper panel* and given in line 1 of Table 7, see Sect. 4.2.2). It is repeated as it is in the other panels to illustrate the variation in the observed spectrum.

Table 4. List of the identified lines in the X-ray spectrum of WR 22.

Ion	Energy (keV)	Type	log T (max) (K)	kT (max) (keV)
Mg XI	1.35	He4	6.8	0.54
Mg XII	1.47	Lyα	7.0	0.86
Si XIII	1.86	He4	7.0	0.86
Si XIV	2.006	Lyα	7.2	1.37
S XV	2.46	He4	7.2	1.37
S XVI	2.62	Lyα	7.4	2.16
S XVI	3.11	Lyβ	7.4	2.16
Ar XVII	3.14	He4	7.3	1.72
Fe K	6.7	K	7.8	5.44

10 MK and the S XV one of 16 MK. This indicates plasma temperatures in the rough range 0.5 keV–1.3 keV.

4.2.1. The combined spectrum

From Fig. 5, it is evident that the hard tail region of the various spectra does not change with time, at least in flux and in slope. Indeed, for each energy bin, all the different datasets agree with each other within their error bars. Consequently, we may hope to get more information on the hard tail by combining all the pointings. Before doing that, we decided to further test the global constancy of the hard tail. We used two methods to check this hypothesis. First, restricting the studied spectra to the photon energy range above 1.7 keV, we tentatively fitted a power law to the data (simultaneously for the three instruments). Even if the power-law model could appear as unphysical, its use is justified by the simplicity of the function, the restricted energy range considered, and the linear appearance of the spectra in this range (see Fig. 5). For the various fittings, we used the XSPEC software (version 11.0). We adjusted the `powerlaw` model and obtained estimated parameters, as well as related χ^2 statistics for the datasets II + VI (simultaneously), VII, III, IV, and V (the interest to use both datasets II and VI simultaneously is explained in Sect. 4.2.2). We also compared the individual observed spectra to the model as fitted to the II+VI dataset (used as a reference). For each dataset (VII, III, IV, and V), we thus obtained a second χ^2 statistics (with the same number of degrees of freedom). The two models can thus be evaluated through direct comparison of the two χ^2 statistics. It turns out that the χ^2 statistics related to the II + VI model are never more than 27% larger than those genuine to the considered dataset. This is not enough to represent a significant deviation, so we conclude that the model fitted on the II + VI dataset is always compatible with the model fitted on the various individual datasets. The slight difference is always explicable by noise fluctuations. As an additional test, we compared, instrument by instrument, the results of the fit of a `powerlaw` (always in the range above 1.7 keV) on the II + VI dataset and on the full dataset II + III + IV + V + VI + VII. The parameters derived from both fits agree well and never differ by more than one standard deviation (on one of the values). Therefore, we can definitively conclude that, within the precision of our data, the hard tail is constant in flux and in apparent slope.

We thus merged the cleaned event lists corresponding to the pointings II to VII taking particular care to maintain the header information about the good time intervals. We extracted X-ray spectra on the basis of the merged lists. The derived MOS spectra are shown in Fig. 6. The three combined spectra (one per EPIC instrument) have no physical meaning in the soft part of the spectrum because of the observed variations at these energies. However, in the constant region of the spectra (typically

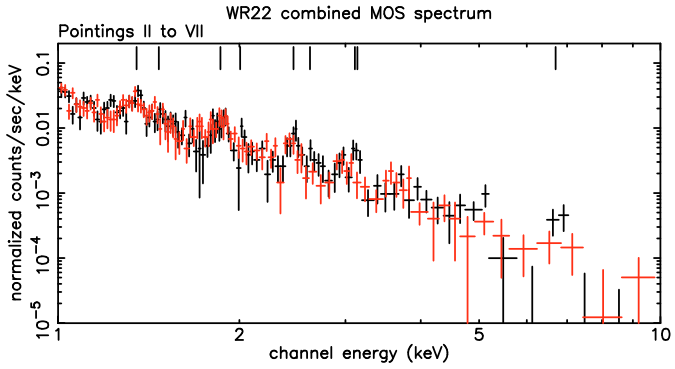

Fig. 6. Combined X-ray spectrum over pointings II to VII (MOS1: black; MOS2: red). This combination is physically meaningful only in the range above about 1.5–2 keV. Thanks to the high signal-to-noise ratio of the combined spectra, emission lines are more easily discernible. Vertical markers indicate the position of the lines listed in Table 4. In particular, let us point out the Fe-K line at ~6.7 keV. Colour indications refer to the electronic version of the paper.

above about 1.5–2 keV), the averaging process must be fully meaningful. The emission lines listed in Table 4 are seen much better in the present spectrum. We can add here the Fe-K line at 6.7 keV, which is clearly present although faint. Though the high-energy tail could obey a power law (except for the presence of the Fe-K line), another component is needed to represent the soft part of the spectrum. The presence of emission lines favours a thermal plasma model. Here and in the following, we decided to use the optically thin thermal plasma model named `mekal` (see Kaastra 1992 and Mewe et al. 1985).

The simultaneous adjustment of a soft `mekal` component and of a `powerlaw` on the combined spectrum above 1 keV leads to a photon index of $2.89^{+0.15}_{-0.23}$, with the soft component necessarily ill-defined. If the fitting is restricted to the range 1–5 keV, a `powerlaw` plus two Gaussian lines at 1.86 keV and at 2.46 keV (in order to take the effect of the cool component into account) give an index of $2.68^{+0.12}_{-0.11}$. The fitting restricted to the 3.5–10 keV region can be performed with a power law characterised by a photon index of $3.52^{+1.80}_{-0.93}$ and a Gaussian at about 6.4–6.7 keV representing the iron line. The values for the photon index derived from these various trials agree internally with each other, so we adopt a median value of 2.99 to represent the power-law slope of the hard tail when necessary. We use this photon index value later to adjust a combined `mekal + powerlaw` model (see Sect. 4.2.2).

The presence of the emission lines and of the Fe-K line, in particular, is a clear indication that the spectrum has a predominantly thermal origin, possibly for the hard tail, too. Consequently, we also fitted a 2-T `mekal` to the combined spectra above 1 keV, and obtained values for the temperature of the hot component in the range 3.2–3.6 keV.

4.2.2. The spectra from pointings II and VI

The spectra corresponding to phases approaching the periastron are rather faint in the soft part, yielding few constraints on the emitting plasma. On the other hand, the observed spectra at phases $\phi = 0.582$ and $\phi = 0.680$ (pointings II and VI) are very similar, indicating that the extinction is also very similar for both pointings (see Fig. 7).

Since they correspond to a comparatively high level of count rates, we may take advantage of these observations to determine the nature of the X-ray emitting plasma at these particular phases. We thus analysed the six spectra (pointings II and VI, and the three instruments), both individually and by groups and, finally, since they yield similar results, all six simultaneously to improve the signal-to-noise ratio. As a first step, we assumed solar abundances for the models and the cross section of neutral gas for the intervening absorbing column as given by the function `wabs` (Morrison & McCammon 1983).

To estimate the interstellar column of neutral hydrogen towards WR 22, we can use the results of Diplas & Savage (1994). According to them, the observed interstellar atomic column density of hydrogen on this line of sight is 0.22×10^{22} cm^{-2}, to which we can add a 12% contribution by molecular hydrogen (see Table 1 of Bohlin et al. 1978). This amounts to 0.25×10^{22} cm^{-2}, which is the value we adopt.

As can be seen in Figs. 5 and 7, the EPIC spectra peak roughly at 0.9 keV, but also possess a hard tail. An absorbed single-temperature, thermal plasma model largely fails to fit the observed spectra. As a next step, we used two-component models of the type `wabs*mekal+wabs*powerlaw` and `wabs*mekal+wabs*mekal`. The absorbing columns were forced to be larger than the minimum value of 0.25×10^{22} cm^{-2} in order to properly take the interstellar medium into account. The resulting fits and the deduced parameters are given in Tables 5 and 6. It is clear that the model `wabs*mekal+wabs*powerlaw` indicates a plasma at 0.6 keV and that the power law is able to explain the hard tail (see Fig. 7). Alternatively, the adjustment of the 2-T `mekal` model suggests the presence of one component at 0.6 keV and of a second one with a less well-determined temperature in the range 1.5–3.5 keV.

We also tentatively fitted Differential Emission Measure composite `mekal` models of the type `wabs*c6pmkl`. This approach clearly suggests a first component in the full range of temperatures 0.3–0.9 keV, but with a well-marked peak centred at 0.55–0.60 keV. This range of temperature agrees rather well with the majority of the lines listed in Table 4. A second clearly detached component is present at 4–6 keV. Therefore, the exact temperature of the hot component remains hard to determine with precision. We tentatively adjusted 3-T `mekal` models: no significant improvement of the fit is observed and the third component is thus not mandatory. However, the newly added component turned out to adopt a low temperature of 0.2 keV. The inclusion of this very cool component has some impact on the observed column densities which we must consider when estimating $N_{\rm H}$ dispersions. It is interesting to notice that the column density at phase 0.5–0.6 is slightly higher than the one expected from the interstellar medium.

4.2.3. The spectra at phases above 0.7

We also analysed the spectra corresponding to the pointings VII, III, IV, V, all related to phases above 0.7. Results of the adjustment of the `wabs1*mekal+wabs2*powerlaw` models are given in Table 5, whereas those concerning the models of the type `wabs1*mekal1+wabs2*mekal2` can be found in Table 6. An inspection of these two tables clearly suggests that the derived models are strongly reminiscent of the one previously deduced from pointings II and VI. In particular, the temperature typical of the main thermal component is rather stable with a value of 0.58–0.62 keV. The major difference from pointing to pointing concerns the column density. When the second component is characterised by a power law (Table 5, first part), the relevant photon index is rather stable in the range 2.4–3.2. The column

Table 5. Results of the fit to the individual X-ray spectra of models of the kind `wabs1*mekal+wabs2*powerlaw`.

No.	Phase	N_{H1} (10^{22} cm^{-2})	kT_1 (keV)	Norm$_1$ (10^{-4} cm^{-5})	N_{H2} (10^{22} cm^{-2})	Ph.I.	Norm$_2$ (10^{-4} cm^{-5})	χ^2_ν	d.o.f.
II+VI	0.582/0.680	$0.37^{+0.11}_{-0.16}$	$0.59^{+0.03}_{-0.03}$	$1.51^{+0.57}_{-0.46}$	$0.30^{+0.40}_{-0.15}$	$2.47^{+0.42}_{-0.18}$	$0.76^{+0.49}_{-0.26}$	1.20	285
VII	0.765	$0.50^{+0.08}_{-0.20}$	$0.60^{+0.04}_{-0.04}$	$1.93^{+0.42}_{-0.90}$	$1.28^{+1.30}_{-0.89}$	$3.01^{+0.36}_{-0.66}$	$1.57^{+3.23}_{-0.77}$	1.07	124
III	0.828	$0.67^{+0.14}_{-0.14}$	$0.58^{+0.05}_{-0.05}$	$2.15^{+1.25}_{-1.01}$	$0.74^{+0.69}_{-0.60}$	$3.21^{+0.24}_{-0.72}$	$2.01^{+1.25}_{-1.27}$	1.34	116
IV	0.903	$1.11^{+0.06}_{-0.30}$	$0.61^{+0.07}_{-0.06}$	$5.72^{+1.98}_{-2.95}$	$4.16^{+9.83}_{-4.53}$	$3.01^{+2.76}_{-2.31}$	2.13^{--}_{--}	1.08	76
V	0.994	$1.58^{+0.26}_{-0.26}$	$0.71^{+0.19}_{-0.12}$	$5.01^{+2.57}_{-2.03}$	$7.08^{+7.17}_{-7.08}$	2.37^{--}_{--}	1.00^{--}_{--}	0.71	38
II+VI	0.582/0.680	$0.31^{+0.04}_{-0.03}$	0.59(fix)	$1.43^{+0.20}_{-0.15}$	$0.82^{+0.36}_{-0.25}$	2.99(fix)	$1.49^{+0.17}_{-0.20}$	1.20	287
VII	0.765	$0.49^{+0.08}_{-0.05}$	0.59(fix)	$1.92^{+0.40}_{-0.32}$	$1.47^{+0.75}_{-0.51}$	2.99(fix)	$1.53^{+0.31}_{-0.24}$	1.05	126
III	0.828	$0.71^{+0.11}_{-0.07}$	0.59(fix)	$2.34^{+1.17}_{-0.47}$	$0.84^{+0.57}_{-0.26}$	2.99(fix)	$1.52^{+0.23}_{-0.26}$	1.32	118
IV	0.903	$1.10^{+0.13}_{-0.13}$	0.59(fix)	$5.61^{+1.46}_{-0.93}$	$3.69^{+3.09}_{-1.84}$	2.99(fix)	$1.98^{+0.46}_{-0.55}$	1.05	78
V	0.994	$1.68^{+0.26}_{-0.27}$	0.59(fix)	$6.99^{+2.46}_{-1.28}$	$7.36^{+6.56}_{-3.40}$	2.99(fix)	$2.53^{+1.87}_{-1.07}$	0.74	40
II+VI	0.582/0.680	$0.39^{+0.02}_{-0.02}$	0.59(fix)	2.00(fix)	$1.11^{+0.13}_{-0.12}$	2.99(fix)	1.51(fix)	1.21	289
VII	0.765	$0.51^{+0.03}_{-0.02}$	0.59(fix)	2.00(fix)	$1.50^{+0.25}_{-0.20}$	2.99(fix)	1.51(fix)	1.03	128
III	0.828	$0.68^{+0.08}_{-0.05}$	0.59(fix)	2.00(fix)	$0.74^{+0.15}_{-0.14}$	2.99(fix)	1.51(fix)	1.30	120
IV	0.903	$0.80^{+0.09}_{-0.06}$	0.59(fix)	2.00(fix)	$1.03^{+0.21}_{-0.19}$	2.99(fix)	1.51(fix)	1.09	80
V	0.994	$1.13^{+0.19}_{-0.12}$	0.59(fix)	2.00(fix)	$1.82^{+0.45}_{-0.35}$	2.99(fix)	1.51(fix)	0.87	42

The first two columns specify the relevant spectrum. Columns 3–5 give respectively the absorbing column density, the plasma temperature and a normalisation factor (norm) equal to $\frac{10^{-14}}{4\pi d^2}\int n_e n_H dV$ with d being the distance to the source (in cm), n_e, n_H the electron and hydrogen number densities respectively (in cm^{-3}). The next three columns are dealing with the second component (power law); the seventh one gives the photon index whereas the eighth one gives the power-law normalisation. The last two columns give the reduced χ^2 of the fit and the number of degrees of freedom. The quoted upper and lower values correspond to the 90% confidence interval (undetermined values are replaced by hyphens).

Table 6. Results of the fit to the individual X-ray spectra of models of the kind `wabs1*mekal1+wabs2*mekal2`. See footnote of Table 5 for details.

No.	Phase	N_{H1} (10^{22} cm^{-2})	kT_1 (keV)	Norm$_1$ (10^{-4} cm^{-5})	N_{H2} (10^{22} cm^{-2})	kT_2 (keV)	Norm$_2$ (10^{-4} cm^{-5})	χ^2_ν	d.o.f.
II+VI	0.582/0.680	$0.42^{+0.03}_{-0.06}$	$0.59^{+0.02}_{-0.02}$	$2.24^{+0.69}_{-0.24}$	$1.16^{+0.90}_{-0.32}$	$2.04^{+0.68}_{-0.80}$	$1.93^{+0.47}_{-0.12}$	1.29	285
VII	0.765	$0.56^{+0.08}_{-0.09}$	$0.59^{+0.04}_{-0.04}$	$2.43^{+0.89}_{-0.85}$	$2.25^{+1.17}_{-0.85}$	$1.58^{+0.45}_{-0.39}$	$2.70^{+4.05}_{-1.20}$	1.08	124
III	0.828	$0.86^{+0.10}_{-0.07}$	$0.59^{+0.05}_{-0.04}$	$4.27^{+1.69}_{-1.49}$	$1.58^{+0.99}_{-0.68}$	$1.81^{+1.09}_{-0.59}$	$2.11^{+1.69}_{-0.91}$	1.40	116
IV	0.903	$1.14^{+0.12}_{-0.15}$	$0.61^{+0.07}_{-0.07}$	$6.10^{+2.09}_{-2.49}$	$5.76^{+8.34}_{-5.95}$	$1.77^{+3.06}_{--}$	$3.56^{+18.4}_{-3.34}$	1.07	76
V	0.994	$1.58^{+0.25}_{-0.26}$	$0.71^{+0.19}_{-0.12}$	$5.04^{+2.52}_{-1.92}$	$7.33^{+18.1}_{--}$	3.45^{--}_{--}	$1.79^{+21.6}_{-1.18}$	0.69	38
II+VI	0.582/0.680	$0.40^{+0.05}_{-0.05}$	$0.59^{+0.02}_{-0.02}$	$1.87^{+0.33}_{-0.37}$	0.25(fix)	$3.71^{+1.11}_{-0.64}$	$1.18^{+0.18}_{-0.17}$	1.28	286
VII	0.765	$0.53^{+0.06}_{-0.07}$	$0.60^{+0.04}_{-0.04}$	$1.88^{+0.87}_{-0.47}$	0.25(fix)	$4.87^{+4.39}_{-1.34}$	$0.95^{+0.20}_{-0.21}$	1.13	125
III	0.828	$0.95^{+0.10}_{-0.11}$	$0.62^{+0.05}_{-0.05}$	$4.49^{+1.14}_{-0.99}$	0.25(fix)	$4.17^{+2.52}_{-1.03}$	$0.86^{+0.24}_{-0.23}$	1.43	117
IV	0.903	$1.07^{+0.13}_{-0.15}$	$0.62^{+0.09}_{-0.09}$	$4.08^{+1.85}_{-1.21}$	0.25(fix)	$7.52^{--}_{-3.80}$	$0.79^{+0.32}_{-0.21}$	1.07	77
V	0.994	$1.58^{+0.22}_{-0.28}$	$0.71^{+0.21}_{-0.16}$	$3.49^{+3.00}_{--}$	0.25(fix)	Undef.	$0.79^{+0.31}_{-0.35}$	0.73	39

density in front of the second component has an ill-defined behaviour, mainly because of the lack of constraint. It is verified in Table 5 (second part) that fixing the temperature of the cool component to 0.59 keV and the photon index to the value 2.99 (as measured on the combined spectrum) does not have too strong an influence on the derived series of column densities. Further fixing the normalisation factor (norm) renders the column density in front of the thermal component slightly less variable with phase (third part). When, in contrast, the second component is assumed to be characterised by a second optically thin thermal plasma, the temperature of the latter ranges from 1.6 to 2.0 keV or even more for pointing V, although this value is not very well defined (see Table 6, first part). The column density in front of the hot component is variable. If we fix this value to the interstellar one, the temperature of the second component generally increases (Table 6, second part). However, the combination of the parameters temperature-column density for the second component has very little impact on the value for the column density in front of the 0.6 keV component. Completely fixing the hot component (not shown here) also has very little impact on the derived characteristics for the first component (except perhaps for pointing V for which the noise is greater). All these trials, and particularly the lack of impact of the choice of the second component on the first one, support the case of a 2-T `mekal` model with a unique absorbing column in front of all the model plasma components (Table 7, first part). We also adjusted 3-T `mekal` models of the type `wabs*(mekal1+mekal2+mekal3)` for reasons similar to those already explained in Sect. 4.2.2. The result of fitting such a model is also given in Table 7 (second part). Finally,

Table 7. Results of the fit to the individual X-ray spectra of models of the type `wabs*(mekal1+mekal2)` (first part of the table) and of the kind `wabs*(mekal1+mekal2+mekal3)` (second and third parts). See footnote of Table 5 for details.

No.	Phase	N_H (10^{22} cm^{-2})	kT_1 (keV)	Norm$_1$ (10^{-4} cm^{-5})	kT_2 (keV)	Norm$_2$ (10^{-4} cm^{-5})	kT_3 (keV)	Norm$_3$ (10^{-4} cm^{-5})	χ^2_ν	d.o.f.
II+VI	0.582/0.680	$0.37^{+0.04}_{-0.04}$	$0.59^{+0.03}_{-0.02}$	$1.78^{+0.31}_{-0.30}$	$3.22^{+0.63}_{-0.44}$	$1.31^{+0.15}_{-0.17}$	–	–	1.29	286
VII	0.765	$0.51^{+0.06}_{-0.10}$	$0.60^{+0.04}_{-0.05}$	$1.85^{+0.97}_{-0.44}$	$3.72^{+2.36}_{-0.87}$	$1.23^{+0.26}_{-0.22}$	–	–	1.15	125
III	0.828	$0.87^{+0.11}_{-0.12}$	$0.60^{+0.05}_{-0.02}$	$4.20^{+1.48}_{-1.34}$	$2.55^{+0.75}_{-0.44}$	$1.39^{+0.36}_{-0.40}$	–	–	1.40	117
IV	0.903	$1.03^{+0.14}_{-0.17}$	$0.61^{+0.08}_{-0.08}$	$4.25^{+1.83}_{-1.72}$	$4.17^{+25.3}_{-1.65}$	$1.14^{+0.48}_{-0.40}$	–	–	1.08	77
V	0.994	$1.47^{+0.29}_{-0.26}$	$0.71^{+0.17}_{-0.14}$	$3.90^{+2.41}_{-1.63}$	Undef.	$0.76^{+0.36}_{-0.33}$	–	–	0.72	39
II+VI	0.582/0.680	$0.58^{+0.06}_{-0.11}$	$0.60^{+0.07}_{-0.03}$	$2.50^{+0.56}_{-1.11}$	$3.64^{+0.96}_{-0.76}$	$1.16^{+0.22}_{-0.17}$	$0.22^{+0.08}_{-0.06}$	$5.08^{+5.27}_{-3.42}$	1.25	284
VII	0.765	$0.65^{+0.16}_{-0.19}$	$0.62^{+0.10}_{-0.05}$	$2.21^{+1.47}_{-0.98}$	$4.01^{+3.03}_{-1.13}$	$1.04^{+0.24}_{-0.25}$	$0.21^{+0.12}_{-0.15}$	$4.21^{+4.76}_{-3.76}$	1.11	123
III	0.828	$1.02^{+0.16}_{-0.20}$	$0.64^{+0.11}_{-0.08}$	$3.75^{+3.74}_{-0.30}$	$2.37^{+0.99}_{-0.45}$	$1.47^{+0.27}_{-0.70}$	$0.18^{+0.06}_{-0.13}$	32.8^{--}_{--}	1.39	115
IV	0.903	$1.20^{+0.45}_{-0.24}$	$0.62^{+0.28}_{-0.14}$	$4.10^{+3.33}_{-2.52}$	$3.69^{+3.40}_{-1.42}$	$1.18^{+0.65}_{-0.52}$	$0.17^{+0.16}_{-0.06}$	61.5^{--}_{--}	1.07	75
V	0.994	$1.79^{+0.98}_{-0.47}$	$0.71^{+0.26}_{-0.20}$	$4.78^{+3.95}_{-2.24}$	Undef.	$0.86^{+0.30}_{-0.82}$	0.11^{--}_{--}	0.25^{--}_{--}	0.71	37
II+VI	0.582/0.680	$0.58^{+0.08}_{-0.11}$	0.60(fix)	$2.50^{+0.32}_{-0.40}$	3.60(fix)	$1.16^{+0.12}_{-0.12}$	0.22(fix)	$5.13^{+4.73}_{-3.32}$	1.24	287
VII	0.765	$0.63^{+0.15}_{-0.16}$	0.60(fix)	$2.17^{+0.54}_{-0.44}$	3.60(fix)	$1.12^{+0.13}_{-0.20}$	0.22(fix)	$3.08^{+3.91}_{-1.53}$	1.09	126
III	0.828	$1.01^{+0.13}_{-0.12}$	0.60(fix)	$5.12^{+1.01}_{-0.94}$	3.60(fix)	$1.02^{+0.19}_{-0.20}$	0.22(fix)	$7.70^{+14.6}_{-6.13}$	1.40	118
IV	0.903	$1.17^{+0.20}_{-0.25}$	0.60(fix)	$4.00^{+1.21}_{-1.16}$	3.60(fix)	$1.21^{+0.29}_{-0.23}$	0.22(fix)	$14.8^{+28.2}_{-14.5}$	1.05	78
V	0.994	$1.56^{+0.52}_{-0.36}$	0.60(fix)	$4.26^{+2.27}_{-1.94}$	3.60(fix)	$1.09^{+0.37}_{-0.37}$	0.22(fix)	$5.42^{+53.5}_{-5.12}$	0.81	40

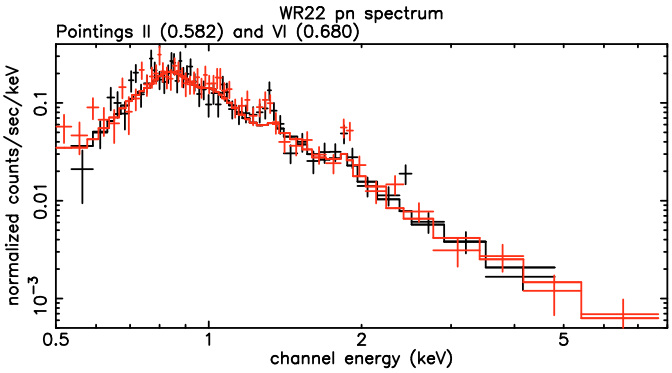

Fig. 7. X-ray spectrum (pn) of WR 22 as observed in pointings II (ϕ = 0.582, black) and VI (ϕ = 0.680, red). The spectra at both phases are very similar. The fitted model is of the type `wabs*mekal+wabs*powerlaw` (line 1 in Table 5). The fit in the hard part is just as good for the 2-T `mekal` model. Colour indications refer to the electronic version of the paper.

we fixed the temperatures of the three `mekal` components to estimate the impact on the column density evolution (Table 7, third part).

4.2.4. The spectrum near apastron (pointing I)

The spectrum acquired during pointing I corresponds to phases near apastron. Only the MOS detectors were usable and the effective exposure time is very low (see Table 2), so that we decided to treat this case separately. The apastron X-ray spectrum is comparable to those of pointings II and VI (see Sect. 4.2.2) in the hard and medium parts (Fig. 5). This conclusion is confirmed by the count rates given in Figs. 3 and 4. The case of the soft part might seem more problematic. However, our apastron spectrum presents only two bins in the soft domain, and these two bins are between 0.7 and 1.0 keV. These two values are also fully compatible with the spectra at phases 0.582 and 0.680. Therefore, the discrepancy suggested in Fig. 4 is an artefact explained by the counts being too low. No other conclusion can be drawn from these data and we will thus not discuss them further.

4.2.5. The evolution of the column density with phase

The main evolution with phase of the column density, as derived from all these fits, is illustrated in Fig. 8. Although we put emphasis on the results given in Table 7 for the `wabs*(mekal1+mekal2)` model, it must be stressed that we have no particular reasons to choose among the various tried models. Therefore, the other results (Tables 5–7) are also plotted in Fig. 8, using the column in front of the 0.6 keV `mekal` component when two independent columns were fitted. The observed dispersion represents the uncertainties in the choice of the model. It is interesting to notice that it remains close to the derived error bars for the `wabs*(mekal1+mekal2)` model. As a conclusion from these results, the analysis of the various spectra confirms the idea that the X-ray emission, or at least its soft part, is absorbed by a material whose column density increases with phase when the O star goes from apastron to periastron. This statement is basically independent of the fitted models. We adopt the 2-T absorbed `mekal` model (Table 7, first part) as the reference for further discussion. It should also be noted that the error bars for the data points at ϕ = 0.582 and 0.680 are artificially small. This is an artefact of the procedure that consisted in performing the fit on both epochs simultaneously. Actually, the true error bars should be $\sqrt{2}$ larger. The typical column densities derived here are not high enough to have any impact on the hard part of the spectrum.

5. Schematic modelling and interpretation

5.1. Origin of the X-ray emission

In a binary system like WR 22, we can identify three possible origins for the X-ray emission. The first one is the intrinsic contribution of the O star. Usually, the emission of such a star can be characterised by a two-temperature (2-T), optically thin, thermal plasma model with $kT_1 \sim 0.2$–0.3 keV and $kT_2 \sim 0.8$ keV

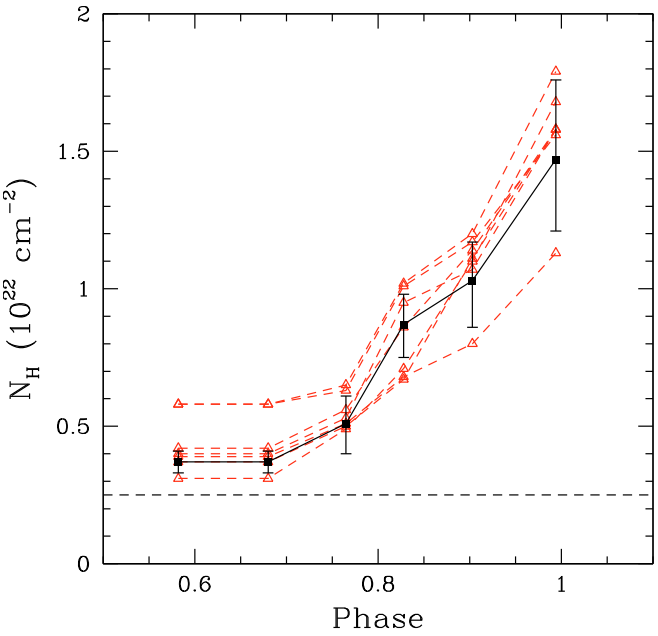

Fig. 8. Evolution of the absorbing column density when WR 22 goes from apastron to periastron. A curve is given for each model of Tables 5–7. They are all indicated by open triangles and dashed lines (red) and they illustrate the dispersion among various models. The bold line in black and the filled squares represent the curve corresponding to the `wabs*(mekal+mekal)` model considered as most representative of the observed phenomenon (error bars represent the 90% confidence interval for this particular fit). The dashed horizontal line represents the interstellar medium contribution. Colour indications refer to the electronic version of the paper.

(see Sana et al. 2006). This type of star is known to emit X-rays proportionally to their bolometric luminosity (Berghöfer et al. 1997; Sana et al. 2006). For a star with a spectral type in the range O7V-O9V, the relation $\log(L_X/L_{bol}) = -6.912$ (see Sana et al. 2006) yields an expected $L_X^O = 0.35\text{–}1.00 \times 10^{32}$ erg s^{-1}. A second contribution to the X-ray emission may be intrinsic to the WR component, although the situation is far less clear in the case of these stars. Wessolowski (1996) demonstrates that some putatively single WR stars were emitting X-rays with luminosities in the range 10^{32}–10^{33} erg s^{-1}. Despite a few efforts, no clear dependence (e.g. with the bolometric luminosity) has been found. As pointed out in the introduction, it could even be that the single WRs emit no X-ray radiation at all. Alternatively, WR 22, which still contains large amounts of hydrogen, represents an evolutionary status that could be reminiscent of a slightly evolved massive O star. Therefore, one could consider that the WR component is following the L_X/L_{bol} relation of O stars, although no observational evidence exists for this idea. If we apply the above relation to WR 22, the $\log L/L_\odot = 5.9$ (Hamann et al. 1995) converts to $L_X \sim 3.7 \times 10^{32}$ erg s^{-1}.

A third contribution is expected from the collision between the two energetic winds. The terminal velocity for the WR wind has been established to be 1785 km s^{-1} (Crowther et al. 1995b, Hamann et al. 2006) and the mass-loss rate has been estimated to $\dot{M}_{WR} \sim 1.6 \times 10^{-5}\, M_\odot$ yr^{-1} from the eclipse study (Rauw 1997). The values for the O star are more difficult to derive; typical values for mid to late O-type stars are $\dot{M}_O \sim 2.8 \times 10^{-7}\, M_\odot$ yr^{-1} and $v_{\infty,O} = 2100$ km s^{-1} (Vink et al. 2001). Since the terminal velocities are quite similar, the dominant effect is the difference in mass-loss rates with the result that the wind of the WR overwhelms that of its O companion (a common occurrence in WR+O systems). The wind collision region is thus expected to wrap itself around the secondary. Following Stevens et al. (1992) and using the assumed parameters summarised in Table 9, we compute the square root of the wind momentum flux ratio $\Re$, which amounts to 6.97. Therefore, the so-called stagnation point occurs near the O star at 12.5% of the orbital separation. According to Stevens et al. (1992), such a ratio also implies a cone opening angle of the collision zone of ∼31° (Eichler & Usov 1993). A 60° opening angle is predicted if one multiplies the mass-loss rate of the O star by an unlikely factor of 10. The distance from the WR star to the shock corresponds to 39.5 R_*^{WR} at apastron and to 11.2 R_*^{WR} at periastron: the wind of the WR star has therefore reached $v_{\infty,WR}$ or nearly so before colliding. However, the wind of the O star might not have the time to reach its terminal velocity before it encounters the WR wind, which further reinforces the preponderance of the latter.

The colliding wind region is broadly characterised by two zones of shocked wind separated by a contact surface. According to Stevens et al. (1992), we may have an idea of the nature of the shock by computing the χ cooling indicator. The χ_{WR} corresponding to the shocked WR wind ranges from 2.1 at apastron to 0.4 at periastron. Therefore, the collision on the WR wind side tends to instead be adiabatic although this is probably not a pure case. On the shocked O star wind side, despite the large dispersion of the χ_O values due to the uncertainties on the O star parameters, we can conclude that the collision is definitely in the adiabatic regime. Provided that the radius of the O star is less than 11 $R_\odot$ (i.e. a typical main sequence star) and assuming a classical $\beta = 1$ velocity law, the wind of the O star reaches 1700 km s^{-1} at apastron and is able to maintain the collision zone away from its surface. This remains the case as long as the wind reaches 1200 km s^{-1}, which happens over the major part of the orbit. In the configuration described above, the shocked WR wind is the dominant source of X-ray emission according to the work of Pittard & Stevens (2002). Near periastron, the O star wind could be difficult to settle and the actual situation is highly dependent on the actual value of the O star radius and also on the details of the velocity law.

At the apex of the collision zone (situated near the binary symmetry axis), the kinetic energy of the matter near the binary axis is converted into heat. Thermalisation in the strong-shock ideal-gas context suggests that the temperature can reach (see Sect. 2.1 of Stevens et al. 1992) about 3.7 keV for solar abundances and even be 50% higher for abundances of the type of those of WR 22. The wind collision region is the only possible phenomenon able to produce such a high temperature and thus a hard tail such as the one seen in the X-ray spectrum. As stated above, the intrinsic O star emission cannot be this hard. It is also in principle the case for the WR star, although a few WR stars usually considered as single, like WR 110 and WR 6 (Skinner et al. 2002a,b), exhibit a hot component[2].

The different zones of emission are observed through an absorbing column because of the interstellar medium, but also through a possible circumstellar and/or wind contribution. In Sect. 5.3, we estimate these column densities. Beforehand, in the next section, we perform a few hydrodynamical simulations to better understand the nature of the colliding wind zone.

[2] Of course, the latter could be due to colliding winds in a yet unrecognised binary system (see the 30 year story of WR 25, Gamen et al. 2006).

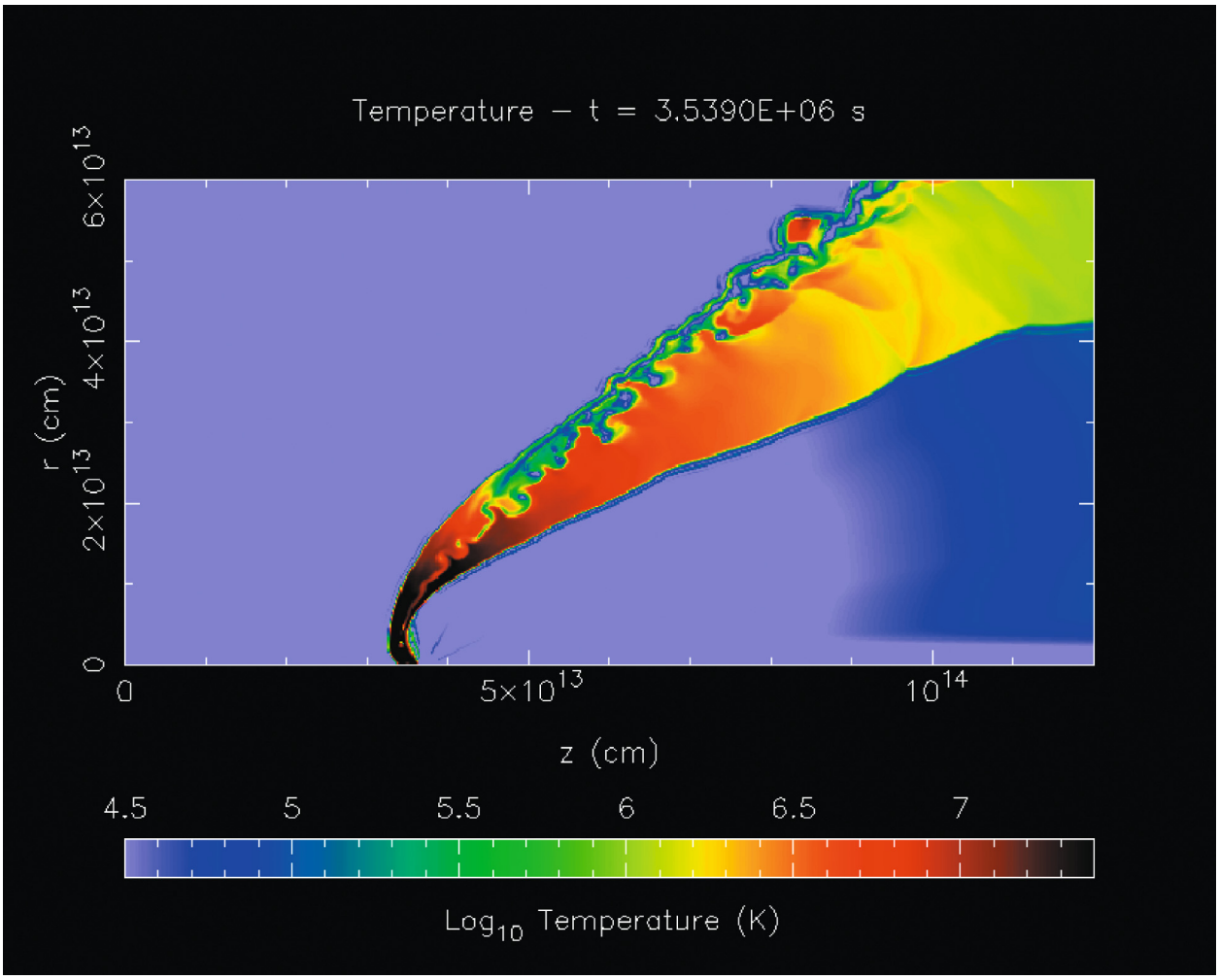

Fig. 9. Hydrodynamical simulations of the colliding winds in the binary system WR 22. The simulation represented here concerns the system at apastron. The WR star is at coordinates (0, 0), whereas the O star is at (3.75×10^{13} cm, 0). The parameter shown here is the temperature due to the shock, so the stars themselves and their wind are not concerned; only the colliding wind region is considered. The temperature is expressed in Kelvin. *t* is the time elapsed since the beginning of the simulations and is long enough that the result is independent of the initial conditions.

5.2. Hydrodynamical simulations

To gain insight into the nature of the wind interaction in WR 22, we closely followed the approach of Stevens et al. (1992), using an adapted version of the VH-1 code to perform numerical simulations of the phenomenon. Owing to the uncertainties on adopted parameters, the following results are only indicative. The numerical code and the benefits and drawbacks of the current approach have been extensively discussed in previous papers and will not be repeated here (see e.g. Sana et al. 2004). We just recall that the winds from the two stars are supposed to be spherically symmetric, fully ionised and of constant velocity. To take advantage of the symmetry of revolution of the problem, we adopted a cylindrical grid whose z-axis matches the binary axis of symmetry (line of centres). All the performed computations were thus done in two dimensions. In the present case, the adopted numerical grid is formed by 600×300 square cells and corresponds to a physical size of $6 \times 3 \times 10^{13}$ cm. In a few instances, we also used twice larger cells. As the VH-1 code is a time-marching algorithm, we let the simulations run for at least 8000 time steps, roughly corresponding, in terms of flow time, to at least 2.2 Ms, long enough to get rid of the perturbations generated by the initial conditions. The three-dimensional X-ray emission generated by the wind interaction was computed at each time step by summing up the emissivity of each grid cell and by accounting for a volume factor resulting from the geometry of the grid. No absorption column, resulting either from the wind material or from the interstellar medium, was taken into account, so that the resulting X-ray luminosity is intrinsic to the wind interaction.

To reasonably cover the range of geometry and of chemical composition encountered in WR 22, we focused on four extreme model configurations that surround the actual system. In the four numerical runs performed, we adopted a separation between the two stars that corresponds either to the apastron passage or to the periastron passage. We also used either a solar composition or a typical WN composition for both winds. For a detailed description of the abundances used, we refer to the work of Stevens et al. (1992). We, however, emphasise that the utilised WN wind composition is actually free of hydrogen so that the actual chemical composition of the hot plasma in WR 22 probably lies between the two extreme cases considered here. Finally, the mass-loss rates and the terminal velocities summarised in Table 9 were used to reproduce the typical strengths of the two winds as closely as possible.

The simulations of the system at apastron (see Fig. 9) confirm the rough analytical estimate of Sect. 5.1, particularly concerning the position of the stagnation point. The shocked WR

Table 8. X-ray luminosities (erg s^{-1}) from the shocked region as predicted by the hydrodynamical simulations.

Abundance En. range	Flux at Apastron	Flux at Periastron
Solar		
[0.5–10.0 keV]	$2.33(\pm0.13) \times 10^{34}$	$6.24(\pm0.92) \times 10^{34}$
[2.0–10.0 keV]	$0.40(\pm0.02) \times 10^{34}$	$0.35(\pm0.07) \times 10^{34}$
WN		
[0.5–10.0 keV]	$1.18(\pm0.09) \times 10^{35}$	$2.44(\pm0.31) \times 10^{35}$
[2.0–10.0 keV]	$1.85(\pm0.12) \times 10^{34}$	$2.14(\pm0.25) \times 10^{34}$

wind near the apex of the collision zone behaves adiabatically. This material reaches temperatures above $\log T(\mathrm{K}) = 7.3$. Farther away from the binary axis, the material flows away and becomes radiative; this happens when the shock zone bends away from the WR to form the cone, which strongly decreases the WR wind velocity component perpendicular to the shock. This is called the effect of shock obliqueness. The shocked O wind remains in the adiabatic regime much farther out. The full width of both collision zones (near the apex) presents a thickness of at least 2×10^{12} cm $\sim 30\ R_\odot$. The contact surface, away from the apex, forms a nicely shaped cone whose opening angle is about $\alpha = 34°$. The WR wind shock zone boundary also forms a cone at an opening angle of $\gamma = 40°$, i.e. $\alpha + 6°$, whereas the one of the O side does the same at $\gamma = 23°$ i.e. $\alpha - 11°$. This configuration is fairly representative of the situation for all the pointings except the one near periastron. At apastron, the whole volume of the collision zone near the apex is filled with rather hot gas ($\log T(\mathrm{K}) > 7.$). This property implies that this part of the collision region has virtually no opacity by itself (Krolik & Kallman 1984).

In the case (not shown here) of the system at periastron, the collision zone near the apex is much thinner and is actually radiative on the WR side of the contact surface. That the hydrodynamical simulations assume a constant pre-shock velocity for the winds implies that the simulations might not be fully representative of the situation at periastron. We have seen above that the O wind could be unable to reach v_∞ before the collision. If this is the case, the WR wind could be crushed onto the O companion surface. However, Gayley et al. (1997) suggest in this particular case that radiative braking could play a significant role by helping the O star keep the collision zone away from its photosphere. The radiative braking in general should further open the angle of the cone and reduce the strength of the shock. In the present simulations, where braking is neglected, it is interesting to notice that the contact surface, away from the apex, forms a nicely shaped cone whose opening angle is about $\alpha = 33°$. Instabilities are clearly seen in the collision zone, particularly on the shocked WR wind side. However, the full collision region is well confined and determined. Both shocked winds should make, at periastron, similar contributions to the X-ray flux according to the work of Pittard & Stevens (2002).

The luminosities from the shocked region, evaluated for these four cases, are given in Table 8. They are computed at apastron and at periastron for both solar abundances and WN ones. The error bars represent 1σ standard deviations corresponding to the natural fluctuations with time of the emission. These luminosities are intrinsic to the colliding winds and fully unabsorbed. The predictions of the hydrodynamical simulations give a genuine luminosity at periastron that is higher by a factor 2.1 to 2.7 (in the total band) than at apastron. However, it is interesting to note that the same ratio is close to unity for the hard band despite the eccentricity of the system: no strong variations are predicted in this band.

Because of the limited nature of some ingredients in the hydrodynamical models, the present simulations should only be considered as illustrative and indicative of what could be expected.

Table 9. Assumed parameters used in computing the models.

Parameter	Adopted value	Explanation
$\dot{M}_{\mathrm{WR}}$	$1.6 \times 10^{-5}\ M_\odot\ \mathrm{yr}^{-1}$	mass-loss rate[a]
$v_{\infty,\mathrm{WR}}$	1785 km s^{-1}	terminal velocity[b,c]
T_*	32 000 K	WR temperature[d]
$v_{0,\mathrm{WR}}$	60 km s^{-1}	initial velocity
R_*^{WR}	11.9 $R_\odot$	stellar radius[a]
$\dot{M}_{\mathrm{O}}$	$2.8 \times 10^{-7}\ M_\odot\ \mathrm{yr}^{-1}$	mass-loss rate[e]
$v_{\infty,\mathrm{O}}$	2100 km s^{-1}	terminal velocity[e]
R_*^{O}	8 to 13 $R_\odot$	stellar radius
i	70° or 85°	System inclination[a] (two test values)

[a] Rauw (1997); [b] Hamann et al. (2006); [c] Crowther et al. (1995b); [d] Lamers & Morris (1994); [e] Vink et al. (2001).

Table 10. Assumed abundances used in computing the wind absorption model.

Parameter	Adopted value	Explanation
$X_{\mathrm{H}}^{\mathrm{WR}}$	0.44	H percentage in mass[f]
$X_{\mathrm{He}}^{\mathrm{WR}}$	0.55	He percentage in mass
$X_{\mathrm{C}}^{\mathrm{WR}}$	3.0×10^{-4}	C percentage in mass
$X_{\mathrm{N}}^{\mathrm{WR}}$	1.0×10^{-2}	N percentage in mass
$X_{\mathrm{O}}^{\mathrm{WR}}$	3.0×10^{-3}	O percentage in mass
$X_{\mathrm{Ne}}^{\mathrm{WR}}$	1.75×10^{-3}	Ne percentage in mass
$X_{\mathrm{Mg}}^{\mathrm{WR}}$	6.53×10^{-4}	Mg percentage in mass
$X_{\mathrm{Si}}^{\mathrm{WR}}$	7.02×10^{-4}	Si percentage in mass
$X_{\mathrm{S}}^{\mathrm{WR}}$	3.67×10^{-4}	S percentage in mass
$X_{\mathrm{Fe}}^{\mathrm{WR}}$	1.84×10^{-3}	Fe percentage in mass
$X_{\mathrm{H}}^{\mathrm{O}}$	0.71	Hydrogen percentage in mass (solar abundances adopted[g])

[f] Crowther et al. (1995a); [g] Anders & Grevesse (1989).

5.3. The intervening absorbing column density

In the present section, we try to interpret the evolution with phase of the observed column density as shown in Fig. 8, on the basis of a simple absorption model. The O star and the colliding wind zone are both expected to be X-ray emission regions. Since the colliding wind zone is estimated to be very close to the O star, we may approximate, as a first step, the actual situation by admitting that the X-ray emission is virtually point-like and located at the position of the O component. Therefore, we derive the optical depth along the line of sight from the O star to the observer avoiding integration over the whole emitting volume. This opacity comes essentially from the WR wind, and we address this problem first. Consequently, we have to consider a chemical composition typical of the WR 22 primary star and, for our computations, we assume the values given in Tables 9 and 10. It should also be noted that, close to the star, the wind is far from neutral, so we decided to include a sound treatment of the ionisation structure of the WR wind in our computations.

We adopted the model of ionisation structure of the wind first developed for O stars (cf. HD 108, Nazé et al. 2004) and inspired by the model of Waldron (1984). The model was adapted to WR stars in Gosset et al. (2005) and is applied here in the case of WR 22. In our model, only the collisional excitation, the photoionisation and the radiative and dielectronic recombinations can affect the ionisation level of an ion. We determined the ionisation structure of the WR wind up to some 400 stellar radii, using the approximations of Waldron (1984) for the radiative field and for the opacities. We used the velocity law $v(r) = v_0 + v_\infty(1 - R_*/r)$ and the wind temperature law $T_{\rm wind}(r) = T_\infty + (T_0 - T_\infty)(R_*/r)^{1.9}$ with $T_\infty = 0.4 \times T_0$ and $T_0 = T_*$ as in Gosset et al. (2005) with the parameters given in Table 9. The temperatures T_* and T_0 have been fixed to 32 000 K (Lamers & Morris 1994; Hamann et al. 1995). The underlying continuum of the star was computed with the WR 22 model used in the analysis of the eclipses, which has been described elsewhere (Rauw 1997).

Once the wind structure of the WR star is computed according to the assumed parameters, all that is left is to integrate the wind along the line of sight (to the observer) from the O star position to a position where the density of the WR wind becomes negligible (we stopped at ~400 $R_*^{\rm WR}$). The work was performed for each position of the O star corresponding to each of the seven pointings. First, we performed the computation in the framework of the Rauw et al. (1996) orbital solution and for an inclination of the system of $i = 85°$. From this model, we derived X-ray optical depths τ_ν (per frequencies, i.e. per individual energy elements) for each pointing. We divided these τ_ν, energy bin per energy bin, by the neutral opacities κ_ν as published by Morrison & McCammon (1983). In such a way, we derived equivalent column densities $M_{\rm H}(\nu)$ (estimates for each photon energy channel). By averaging these column densities over the range of frequencies (energies) covered by the studied part of the *XMM-Newton* spectrum, we obtained average column densities $M_{\rm H}$ directly comparable to the column densities derived with XSPEC in the previous section. This is clearly an approximation, since the averaging process is dominated by the region around 1 keV and does not take the ionisation edges present in the opacity spectrum into account. However, most of the differences between neutral gas opacities and ionised ones occur at the ionisation edges located below 1.0 keV. Finally, we added to the computed column densities the column $N_{\rm H}^{\rm ism} = 0.25 \times 10^{22}$ cm^{-2} (see Sect. 4.2.2) corresponding to the interstellar medium. In Fig. 10, we plot these transformed model column densities as a function of the phase of the binary system, along with the column densities derived from the observations. It is immediately obvious that the model column densities are higher than the derived ones. The values are generally comparable at phase $\phi = 0.828$, but they are clearly different at phases $\phi = 0.582$ and 0.680. However, the opening angle of the cone formed by the collision zone is expected to be at least 31°–34°. If confirmed, the O star and the X-rays from the wind collision zone are thus seen, at these two phases, through the interior of the cone, which is filled by the O wind, and the absorption is thus dominated by lower density material with solar abundances.

From previous works on the opacity of O star winds (see in particular HD 108, Nazé et al. 2004), we estimate the column density above the X-ray emitting plasma of a typical O star wind to be $N_{\rm H,O} \sim 0.25 \times 10^{22}$ cm^{-2}. If the X-ray emission comes from the O star, the radiation goes through this material before leaving the system. If the emission comes from a location close to the apex, between the WR and the O stars, we should observe a somewhat higher column density (less than twice the quoted value). These values need to be cumulated with the interstellar column density which is of order of $N_{\rm H}^{\rm ism} = 0.25 \times 10^{22}$ cm^{-2}. The observed value in excess of the interstellar-medium contribution seems to be at least a factor of two lower (Fig. 10). Therefore, the dominating source of X-rays could not be restricted to the binary axis locus between the WR and the O stars. It could not be intrinsic either to the O component, except if the X-ray emitting plasma in the O star wind is located farther out than generally admitted. To obtain a local column density lower than $N_{\rm H} = 0.25 \times 10^{22}$ cm^{-2}, the X-ray emission originating in the colliding wind zone should follow a path to the observer that has an impact distance from the O star of more than 5–6 $R_*^{\rm O}$ (O star radius). For example, a radius of the O star of 10 $R_\odot$ (~main sequence) gives a distance of 3.5–4.0 $\times 10^{12}$ cm. This value agrees fairly well with corresponding dimensions as determined for γ^2 Vel (Henley et al. 2005), as well as by our present simulations. Generally, the line of centres is inclined with respect to the line of sight (orbital phase and inclination). However, at $\phi = 0.680$, the impact distance of the line of sight to the stagnation point remains less than 5–6 $R_*^{\rm O}$. Therefore, the extension of the emitting volume must be the correct interpretation for the low extinction value (pointings I, II, and VI).

The pointing at $\phi = 0.765$ is much more difficult to treat because the line of sight could only be partly within the cone. In such a case, the X-ray photons travel first through part of the O-star wind and afterwards through the external part of the WR wind. Therefore, the actual value of the column density should be located somewhere between the O star effect considered above and the effect of the WR wind. Actually, the WR wind model predicts a value that should be decreased by some 53% to reproduce the observationally derived column density. Finally at phases $\phi = 0.828$ and beyond, the line of sight

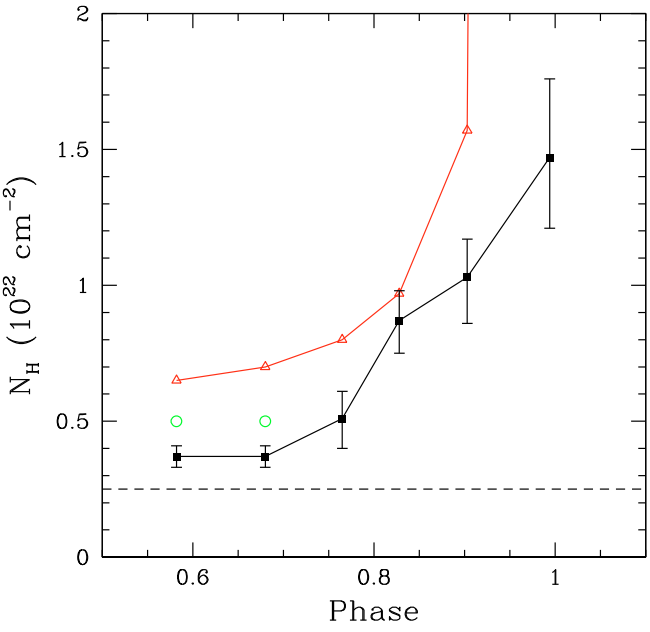

Fig. 10. Comparison of the observationally derived column densities with those predicted by our simple schematic model of the WR wind. The squares (black) represent the derived column densities, the triangles (red) the computed ones ($M_{\rm H}$). At phase $\phi = 0.994$, the predicted value for the column density goes up to 43.6×10^{22} cm^{-2} and is out of the figure. The two circles (green) represent the intrinsic column density of the O star wind complemented by the interstellar medium contribution, which is represented by the dashed line. Colour indications refer to the electronic version of the paper.

opacity is essentially caused by the WR wind. The model value for the equivalent column density should be decreased by a mere 14% at $\phi = 0.828$ to fit the derived value, and we consider that this point is reasonably interpreted by our simple model. However, the situation becomes worse towards periastron. At phase $\phi = 0.903$, the prediction should be decreased by 40% (which is still affordable), but for pointing V ($\phi = 0.994$), a 97% decrease is needed. The interpretation of this near-periastron observation is clearly problematic. The situation is particularly bad in the case of the Rauw et al. (1996) orbit, because the pointing V coincides with the optical eclipse, and the eclipse effect by the core of the WR itself is not even taken into account in the present computations. Therefore, while for all the other pointings, a reduction of the optical depth of 14 to 50% would most probably bring the model in concordance with the observations, the observation related to the pointing near periastron indicates a deep mismatch with the model.

5.4. A more rigorous approach

In the previous section, we transformed the computed optical depths of the wind into equivalent column densities $N_{\rm H}$ (solar abundances) by dividing by the opacities for neutral material. This is clearly an approximation that has the advantage of allowing a rapid comparison with the fitted column densities. In the present section, we adopt a more rigorous approach whose first step consists in introducing actual hydrogen column densities. Indeed, the WR wind is expected to have a chemical composition related to the WR star. We thus introduce the definition

$$N_{\rm W} = \frac{X_{\rm H}}{m_{\rm H}} \int \rho(\mathrm{r})\ \mathrm{d}r \qquad (1)$$

where $X_{\rm H}$ is the actual abundance by mass of hydrogen and $m_{\rm H}$ the mass of an H atom. Using $X_{\rm H} = 0.44$ allows us to define true column densities. Again, we computed these $N_{\rm W}$ integral column densities for each line of sight. Also, for each line of sight, we are thus able to compute the corresponding mean opacities per individual energy channels by dividing the optical depths, per individual energy channels, by the relevant $N_{\rm W}$. The collision zone is expected to be transparent. Since this region is likely to be small, we did not take the effect into account in the computation. It is interesting to notice that the computed opacities are not very different from line of sight to line of sight. The main effect that differentiates the various optical depths is the actual column density, whereas the ionisation structure remains a secondary factor. The computed mean opacities do not differ by more than 16% from one line of sight to the other in the total energy band covered by the spectrum. This conclusion is of course restricted to the framework of the WR wind models.

In Table 11, we report the computed column densities for all seven pointings. The columns are in units of 10^{22} cm^{-2} and correspond to the chemical composition of the WR wind (see Table 10). The column densities were computed for the orbital solutions of Schweickhardt et al. (1999, noted S) and of Rauw et al. (1996, noted R), and for inclinations of the system of 70° and 85°. The solution R85 is adopted for comparison and we transformed the value (Col. 7) in approximately equivalent column densities for solar abundances, by correcting for the normalisation in the H content. From this table, we can conclude that a) the computed WR wind column densities are not at all dependent on the adopted inclination in the range compatible with the results from the optical eclipse analysis except for the periastron pointing where going from $i = 85°$ to $i = 70°$ might help to reduce the column by a factor 2 to 3; b) the choice of the orbital solution has virtually no impact on the conclusions of the present analysis except perhaps (and again) for the periastron pointing and the eclipse.

Table 11. Column densities deduced from the model described in Sect. 5.4, as a function of the phase of the system. The columns are in units of 10^{22} cm^{-2}.

No.	Phase	$N_{\rm W}$ S70	$N_{\rm W}$ R70	$N_{\rm W}$ S85	$N_{\rm W}$ R85	$\sim N_{\rm H}$ R85	$N_{\rm W}$ Obs.	Fraction
I	0.497	0.30	0.28	0.32	0.30	0.48	0.126	(0.43)
II	0.582	0.31	0.29	0.32	0.30	0.49	0.135	(0.44)
VI	0.680	0.34	0.33	0.36	0.34	0.55	0.135	(0.40)
VII	0.765	0.41	0.39	0.43	0.41	0.66	0.234	0.57
III	0.828	0.51	0.50	0.53	0.52	0.84	0.501	0.96
IV	0.903	0.85	0.86	0.90	0.91	1.46	0.575	0.63
V	0.994	9.33	8.54	20.9	28.9	46.5	0.832	0.03

The second step towards a more rigorous way to compare the models to the observations is to directly make use of the mean opacities (per individual energy channels). They represent some kind of weighted effect averaged over the particular line of sight. Therefore, with each pointing we associate the relevant averaged opacities per individual energy channels, as well as the computed column density that is used as a normalisation factor. We then introduced these opacity tables in FITS files that can be used by XSPEC. Thus, within XSPEC, we adopted a model of the type $\texttt{wabs}_{\rm ism}*\texttt{wind}_{\rm WR}*\texttt{(mekal1 + mekal2)}$, where $\texttt{wabs}_{\rm ism}$ deals with the interstellar absorption, which is fixed to $N_{\rm H}^{\rm ism} = 0.25 \times 10^{22}$ cm^{-2}. The term $\texttt{wind}_{\rm WR}$ represents our opacities computed with the WR 22 chemical composition. The adjustment of this model to the observed X-ray spectra allows us to derive column densities $N_{\rm W}$ that are directly comparable to our theoretical column densities. In Table 11 (eighth column), we give the observationally derived column densities $N_{\rm W}$ as resulting from the fits to the data in the case of the Rauw et al. (1996) orbital solution and of the most probable inclination $i = 85°$. We also provide in the last column the fraction that the derived column represents compared to the theoretical ones (R85 case). Concerning the pointings I, II and VI, the figures are given for comparison and are in parentheses to recall that the exact treatment has nothing to do with the WR wind but is rather relevant to the O one. It is important to notice that the two `mekal` components are virtually identical to those reported in Table 7; in particular, the temperatures remained perfectly unchanged. We also considered that the emitting plasma could be non solar in composition. Therefore, we adopted the chemical composition of WR 22 (Table 10) for both `mekal` (actually `vmekal`) components, and fitted the observed spectra again. The column densities derived this way are exactly the same, suggesting some robustness of our derived values. The deduced temperatures did not change either by more than 10%, making our conclusions more robust.

Clearly, this more rigorous approach confirms the previous results: the model is absorbing too much and a decrease in the theoretical optical depth is suggested. These conclusions are fully independent of the abundances used for the emitting plasma. To reduce the total optical depth along the line of sight, we tried to adjust a few model parameters. The column density changes by adjusting the following parameters: $\dot{M}_{\rm WR}$, $v_{\infty,\rm WR}$, and $R_*^{\rm WR}$. The terminal velocity of the WR star is an observed value known with some confidence. It cannot be modified much and is certainly not able to explain the discrepancy. Modifying the star radius will have some impact, particularly near the stellar surface. However, the adopted radius is already relatively small for

Table 12. Observed, ism corrected and totally unabsorbed fluxes of WR 22 in the different energy bands. The fluxes are expressed in 10^{-13} erg cm^{-2} s^{-1}.

Energy band (keV)	ϕ = 0.582/0.680 II+VI	ϕ = 0.765 VII	ϕ = 0.828 III	ϕ = 0.903 IV	ϕ = 0.994 V
Observed fluxes					
0.5–10.0	3.00	2.46	2.35	2.21	1.77
0.5–1.0	0.87	0.55	0.35	0.22	0.05
1.0–2.0	1.02	0.82	1.00	0.79	0.47
2.0–10.0	1.12	1.08	1.00	1.20	1.23
ism corrected fluxes					
0.5–10.0	4.83	3.62	3.22	2.82	2.01
0.5–1.0	2.28	1.38	0.84	0.53	0.11
1.0–2.0	1.42	1.15	1.35	1.08	0.61
2.0–10.0	1.13	1.09	1.03	1.21	1.28
Unabsorbed fluxes					
0.5–10.0	7.36	7.20	14.27	13.17	11.11
0.5–1.0	4.34	4.27	9.54	8.58	6.75
1.0–2.0	1.84	1.77	3.59	3.22	2.91
2.0–10.0	1.18	1.16	1.15	1.22	1.45

such a star, and increasing it will have the opposite effect on the column density. Therefore, the sole degree of freedom we have is on $\dot{M}_{\rm WR}$. A modification of the computed opacity is also a possibility. To reduce it, we computed an alternative model with a temperature T_* for the WR star of 45 000 K instead of 32 000 K. This decreases the opacity by about 2% at 0.5 keV and 6% at 0.3 keV, which is again insufficient.

Adjusting the parameter $\dot{M}_{\rm WR}$ allows us to tie in the model to the X-ray observations, but the discrepancy associated to the near-periastron pointing (V at $\phi = 0.994$) does remain. As noted above, the hard X-ray emission is constant and not affected by the eclipse phenomenon. However, if we enlarge the emission region, part of the X-ray photons on their way to the observer will avoid the core of the WR and will cross the WR wind through regions of lower densities. Therefore, to explain the lack of variations, the core of the WR star should not represent more than 5 to 10% of the emitting volume projected on a plane perpendicular to the line of sight. Approximating the latter surface by a circle means that the corresponding radius should be of the order of 3.1–4.5 $R_*^{\rm WR}$ (i.e. 2.6–3.7 $\times 10^{12}$ cm $\sim$ 37–53 $R_\odot$). In addition to the eclipse phenomenon, the observationally derived column density associated to the pointing V only represents 3% of the theoretical one. Again, the extension of the X-ray emitting zone (compared to its point-like nature in the model) may explain the low value for the derived column. The present deductions are particularly relevant to the soft emission component. Actually, to reach the observed value, it is necessary to extend the volume of the X-ray emission to a radius strictly larger than 20 $R_*^{\rm WR}$ (i.e. 1.7×10^{13} cm $\sim$244 $R_\odot$). Such an extension does not contradict the predictions of the hydrodynamical simulations.

5.5. The X-ray luminosity of WR 22

Assuming that the singly absorbed 2-T `mekal` (cf. Table 7) is the most representative model, we derived the observed X-ray fluxes for WR 22. These are given in the first part of Table 12 for various bands. They are expressed in 10^{-13} erg cm^{-2} s^{-1}. They were deduced by fitting the 2-T `mekal` model absorbed with the interstellar column and the observed effect of the WR wind. They concern the fit performed with the WR 22 composition and the rigorous approach. We further computed the ism corrected fluxes and those corrected for the total observed column densities. These results are also shown in Table 12. The errors on the observed and ism corrected fluxes should be of the order of 10–20%. It should be clear that the computation of the unabsorbed fluxes implicitly assumes that all the X-ray emission originates in the same physical region. Since this is not obvious, one should be very cautious when using these figures.

At maximum, the dereddened flux of WR 22 is $f_{\rm X}^{\rm WR\ 22}(0.5{-}10.0\,{\rm keV}) = 4.83 \times 10^{-13}$ erg cm^{-2} s^{-1} and the luminosity is thus $L_{\rm X}^{\rm WR\ 22}(0.5{-}10.0\,{\rm keV}) = 4.2 \times 10^{32}$ erg s^{-1} (ism corrected). This is much more than what is expected for the O star alone and indicates that there is an additional source of X-rays: the wind collision. The conclusion remains valid even if we add the maximum contribution acceptable for the WR star (see the discussion below).

Along the X-ray lightcurve, the observed flux in the total band decreases from apastron to periastron, and it is clear that this is mainly due to the soft band. The long-term stability of the X-ray lightcurve should also be underlined. Indeed, Pollock (1987) reported *EINSTEIN* observations of WR 22 at phases 0.56 and 0.07. We used the adopted 2-T `mekal` model and the fluxes as given in Table 12 at $\phi = 0.582$ and $\phi = 0.994$ to estimate *EINSTEIN* count rates. We obtain 11.3×10^{-3} and 3.1×10^{-3} counts s^{-1} to be compared to $11{-}13 \times 10^{-3}$ and 3×10^{-3} counts s^{-1}, as reported by Pollock, indicating a long-term stability.

In the framework of the proposed model, it is interesting to estimate the X-ray emission coming from the plasma below the absorbing column attributable to the winds. However, the situation concerning the unabsorbed fluxes and the soft band is not straightforward. Indeed, there seem to be two values for the unabsorbed fluxes. For phases lower than 0.8, we deduce $f_{\rm X}^{\rm unabs}(0.5{-}1.0\,{\rm keV}) = 4.3 \times 10^{-13}$ erg cm^{-2} s^{-1} and $f_{\rm X}^{\rm unabs}(0.5{-}10.0\,{\rm keV}) = 7.3 \times 10^{-13}$ erg cm^{-2} s^{-1}, whereas for phases larger than 0.8, we arrive at $f_{\rm X}^{\rm unabs}(0.5{-}1.0\,{\rm keV}) = 9.0 \times 10^{-13}$ erg cm^{-2} s^{-1} and $f_{\rm X}^{\rm unabs}(0.5{-}10.0\,{\rm keV}) = 13.0 \times 10^{-13}$ erg cm^{-2} s^{-1}. This occurs because the best fits as reported e.g. in Table 7 exhibit a larger norm (about twice) for phases larger than 0.8. A change of the norm is not mandatory in our simple model. The change in the norm (i.e. in the amount of emitting matter) could be real (and actually this is the best fit), although it could be the result of the large uncertainties on the norm due to the low signal-to-noise ratio. We consider this range of values as representative of

a genuine uncertainty. Consequently, we deduce fully unabsorbed luminosities $L_X(0.5{-}10.0\,\mathrm{keV}) = 6.4{-}11.3\times10^{32}$ erg s^{-1} and $L_X(0.5-1.0\,\mathrm{keV}) = 3.7{-}7.8\times10^{32}$ erg s^{-1}. Even using the highest luminosity in the total band, the obtained value is far below the prediction of the simulations, which suggest at least $L_X(0.5{-}10.0\,\mathrm{keV}) = 2.3\times10^{34}$ erg s^{-1}. Using the formalism of Usov (1992), we obtain the theoretical luminosities L_X(apastron) $= 1.4\times10^{33}$ erg s^{-1} and L_X(periastron) $= 4.8\times10^{33}$ erg s^{-1}, which are in better agreement, although still too high.

A discrepancy thus exists between the observations and theory, this is even truer since the observed X-ray luminosity of WR 22 should also contain a contribution from the O star and possibly even one from the WR itself. To better evaluate this discrepancy, we prefer to work in the hard band that is dominated by the collision phenomenon. In this hard band, we derive a constant flux $f_X(2.0{-}10.0\,\mathrm{keV}) = 1.1{\times}10^{-13}$ erg cm^{-2} s^{-1}. The corresponding unabsorbed flux is $f_X^{\mathrm{unabs}}(2.0{-}10.0\,\mathrm{keV}) = 1.2\times10^{-13}$ erg cm^{-2} s^{-1}. Starting from the totally unabsorbed fluxes, we computed the unabsorbed luminosity fully attributed to the colliding wind region in the hard band $L_X^{\mathrm{CW}}(2.0{-}10.0\,\mathrm{keV}) = 1.05\times10^{32}$ erg s^{-1}. This value is more reliable because the correction for the absorbing column is much smaller. However, this observationally derived value is still at least 30 times lower than what is predicted in Sect. 5.2 (Table 8) and at least 10 times lower compared to the Usov (1992) formalism. We consider this constraint as an indicative restriction for the CW models.

Concerning relative variations of fluxes, both the hydrodynamical simulations and the Usov formalism predict that the collision region should be 2 to 3 times more luminous (in the total band) at periastron than at apastron. Although the effect could be present in the soft band, the uncertainty in the observations prevents any firm conclusions. However, considering the hard band, which is dominated by the colliding wind phenomenon, no strong change is predicted, in good agreement with the present observations.

As a final step, we would like to emphasise that, up to now, we have assumed that the WR component was not intrinsically emitting X-rays. If the WR star were emitting X-rays, these would appear as an additional constant contribution all over the orbital cycle (except when the line of sight to the WR crosses the O wind inside the cone instead of the WR wind). This additional contribution to the flux would dilute the extinction phenomenon. Therefore, generally, the observed column densities mentioned above can be considered as lower limits. It is possible to constrain the intrinsic emission of the WR by taking the pointing V whose soft component is at a minimum into account. To obtain an upper limit on the luminosity of the WR component of WR 22, we consider that the soft emission seen at the time of pointing V is entirely due to the WR. Although this is unlikely to be the case, it leads to a firm upper limit. We fitted the relevant spectrum with a 2-T `mekal` model characterised by $kT_1 = 0.6$ keV and a hotter component.

The flux in the soft band is dominated by the cool component to which we attribute a flux $f_X^{\mathrm{obs}}(0.5{-}1.0\,\mathrm{keV}) = 0.05\times10^{-13}$ erg cm^{-2} s^{-1} (see pointing V, Table 12). Correcting it for the interstellar column, we obtained a flux that we consider intrinsic to the WR $f_X^{\mathrm{int.WR}}(0.5{-}1.0\,\mathrm{keV}) = 0.1\times10^{-13}$ erg cm^{-2} s^{-1}, leading to $L_X^{\mathrm{WR}}(0.5{-}1.0\,\mathrm{keV}) < 9.2\times10^{30}$ erg s^{-1} and $\log L_X/L_{\mathrm{bol}} < -8.5$ (restricted to the soft band).

Another approach is to consider that the residual cool component is entirely due to the WR. In the total energy band, the observed flux associated with the cool component at pointing V is $f_X^{\mathrm{obs}}(0.5{-}10.0\,\mathrm{keV}) = 0.59\times10^{-13}$ erg cm^{-2} s^{-1} and, after correction for the ism, we obtain $f_X^{\mathrm{int.WR}}(0.5{-}10.0\,\mathrm{keV}) = 0.76\times10^{-13}$ erg cm^{-2} s^{-1}. For the total band, a less restrictive upper limit is thus $L_X^{\mathrm{WR}}(0.5{-}10.0\,\mathrm{keV}) < 6.6\times10^{31}$ erg s^{-1} and $\log L_X/L_{\mathrm{bol}} < -7.7$. This second limit relies on the hypothesis that the WR emits similarly to the 0.6 keV component.

These limits are very similar to those derived on the basis of not detect WR 40 (Gosset et al. 2005) and are certainly another example of the question of the existence of an intrinsic X-ray emission in single WR stars (see also Oskinova et al. 2003; Skinner et al. 2006).

6. Conclusions

We performed phase-resolved X-ray observations of the exceptionally massive WN+O binary WR 22 with the *XMM-Newton* facility. We observed the system at seven different phases between near apastron, when the O star is roughly in front, to near periastron, when the WR eclipses its companion. The X-ray spectrum can be modelled by at least a two-temperature, optically thin, thermal plasma with $kT_1 = 0.6$ keV and another hot component in the range 2.0–4.5 keV (see Table 7). The decomposition is remarkably similar to what has been observed for various other WRs (WR 110, Skinner et al. 2002a; WR 6, Skinner et al. 2002b; WR 25, Raassen et al. 2003; Pollock & Corcoran 2006). The hot component usually indicates a colliding wind phenomenon that is expected for such a binary.

When the system goes from apastron to periastron, the hard part of the observed spectrum remains constant, whereas the soft part progressively decreases. This can be explained by an increasing absorption column in front of the major part of the emitting plasma. We have demonstrated that this behaviour can be qualitatively interpreted by an X-ray emission partly intrinsic to the O star, but also caused by an accompanying, extended colliding wind region (most probably shaped like a cone) with an apex very close to the O star. We showed that the latter phenomenon is dominant; therefore, when the star goes from apastron to periastron, the X-ray emitting plasma actually sinks deeper and deeper into the WR wind, explaining the observed increasing absorption. We derived observed column densities at each observing phase and showed their rather smooth increase with it. We built up a simple model of the WR wind with a mass-loss rate of $1.6\times10^{-5}\,M_\odot$ yr^{-1} that represents the general trend of the observations rather well, although some discrepancies remain. For the three pointings nearest to apastron, the observationally derived column density has a weaker effect than the expected extinction due to the modelled WR wind. This can be explained by the CW zone forming a cone whose opening angle is predicted to be around 31° and that is wrapped around the O star. At these phases, the X-ray emitting plasma is not seen through the WR wind but through the less opaque O wind inside the cone. We note that, in the case of WR 22, the orbital configuration and the wind parameters lead to a situation where the signature of the cone is not as obvious as in systems such as γ^2 Vel (Schild et al. 2004; Henley et al. 2005).

For the positions somewhat later in phase, our model predicts column densities that are either, within the noise, in good agreement with the observations, or should still be reduced by up to 40%. This discrepancy is less than the uncertainties on the mass-loss rates and does not challenge the general scheme. Either the model could be too simple to fit the data perfectly (for example, porosity of the wind is not considered; it is certainly beyond the scope of the present observational paper to

improve the model) or the adopted mass-loss rate is too high (it is deduced from the analysis of the eclipses in the visible domain and is already a significant lowering of the values $\dot{M}_{\rm spec}$ = 4–12 × 10^{-5} $M_\odot$ $\rm yr^{-1}$ deduced from the analysis of the UV/visible/IR spectra; Hamann et al. 1995; Crowther et al. 1995a; Hamann et al. 2006). The difference in mass-loss rates could be explained by a clumping factor (inverse of the volume filling factor) between 6 and 50 (the D in Hamann et al. 2006). A last possibility is that the WR star does contribute to the X-ray emission, which would then act as a third light. Observationally derived columns would then be lower limits of the actual column towards the O star.

From the faintest observed spectrum (the one near periastron), we derived an upper limit on the WR luminosity by assuming that all the remaining soft flux is actually originating in the WR: this suggests an $L_{\rm X}/L_{\rm bol}$ ratio that is at least an order of magnitude lower than the value obtained by applying the O-star scaling law ($\log L_{\rm X}/L_{\rm bol} = -6.912$).

Near periastron, very large absorption columns are expected as the WR nearly eclipses its companion. The derived column density values are much lower than predicted. This suggests that the X-ray emitting region is extended. The hard X-ray emitting collision zone should have a typical size (radius) of 50–60 $R_\odot$, whereas the typical size corresponding to the soft emission is expected to be at least 244 $R_\odot$. These values are in rather good agreement with the hydrodynamical simulations.

WR 22 is a very interesting object and we showed here that the O star on its orbit around the WR component allows us to scan the wind of the WR star in the X-ray domain. Although faint in X-rays, this object is a promising target for future high-resolution X-ray spectroscopy aiming at further probing the WR wind structure. This will become possible with the next generation of X-ray observatories.

Acknowledgements. We are grateful to the Belgian FNRS for several sources of support. We also acknowledge financial support through the XMM-OM, the XMM and the INTEGRAL PRODEX contracts, as well as through the PAI contract P5/36 (Belspo). Finally, a recent contract by the Communauté Française de Belgique (Action de Recherche Concertée)- Académie Wallonie-Europe is also acknowledged.

References

Anders, E., & Grevesse, N. 1989, Geochem. Cosmochim. Acta, 53, 197
Balona, L.A., Egan, J., & Marang, F. 1989, MNRAS, 240, 103
Berghöfer, T. W., Schmitt, J. H. M. M., Danner, R., & Cassinelli, J. P. 1997, A&A, 322, 167
Bohlin, R. C., Savage, B. D., & Drake, J. F. 1978, ApJ, 224, 132
Cherepashchuk, A. M. 1976, Sov. Astr. Lett., 2, 138
Chlebowski, T., & Garmany, C. D. 1991, ApJ, 368, 241
Claeskens, J. F., Gosset, E., Nazé, Y., Rauw, G., & Vreux, J. M. 2009, submitted
Conti, P. S., Niemela, V. S., & Walborn, N. R. 1979, ApJ, 228, 206
Crowther, P. A., Hillier, D. J., & Smith, L. J. 1995a, A&A, 293, 403
Crowther, P. A., Hillier, D. J., Smith, L. J., & Schmutz, W. 1995b, A&A, 293, 427
De Becker, M., Rauw, G., Pittard, J. M., et al. 2004, A&A, 416, 221
den Herder, J. W., Brinkman, A. C., Kahn, S. M., et al. 2001, A&A, 365, L7
Diplas, A., & Savage, B. D. 1994, ApJS, 93, 211
Eichler, D., & Usov, V. 1993, ApJ, 402, 271
Gayley, K. G., Owocki, S. P., & Cranmer, S. R. 1997, ApJ, 475, 786
Gamen, R., Gosset, E., Morrell, N., et al. 2006, A&A, 460, 777
Gosset, E., Remy, M., Manfroid, J., et al. 1991, IBVS, 3571, 1
Gosset, E., Nazé, Y., Claeskens, J. F., et al. 2005, A&A, 429, 685
Hamann, W. R., Duennebel, G., Koesterke, L., Wessolowski, U., & Schmutz, W. 1991, A&A, 249, 443
Hamann, W. R., Koesterke, L., & Wessolowski, U. 1995, A&A, 299, 151
Hamann, W. R., Gräfener, G., & Liermann, A. 2006, A&A, 457, 1015
Harnden, F. R. Jr., Branduardi, G., Elvis, M., et al. 1979, ApJ, 234, L51
Henley, D. B., Stevens, I. R., & Pittard, J. M. 2005, MNRAS, 356, 1308
Howarth, I. D., & Prinja, R. K. 1989, ApJS, 69, 527
Ignace, R., & Oskinova, L. M. 1999, A&A, 348, L45
Jansen, F., Lumb, D., Altieri, B., et al. 2001, A&A, 365, L1
Johnson, H. L., Iriarte, B., Mitchell, R. I., & Wisniewski, W. Z. 1966, Comm. Lunar Plan. Lab., 4, 99
Kaastra, J. S. 1992, An X-ray spectral code for optically thin plasmas, Internal SRON-Leiden Report
Krolik, J. H., & Kallman, T. R. 1984, ApJ, 286, 366
Lamers, H. J. G. L. M., & Morris, P. W. 1994, private communication
Lundström, I., & Stenholm, B. 1984, A&AS, 58, 163
Mason, K. O., Breeveld, A., Much, R., et al. 2001, A&A, 365, L36
Mewe, R., Gronenschild, E. H. B. M., & van den Oord, G. H. J. 1985, A&AS, 62, 197
Moffat, A. F. J., & Seggewiss, W. 1978, A&A, 70, 69
Morrison, R., & McCammon, D. 1983, ApJ, 270, 119
Nazé, Y., Rauw, G., Vreux, J.-M., & De Becker, M. 2004, A&A, 417, 667
Niemela, V. S. 1973, PASP, 85, 220
Niemela, V. S. 1979, in Mass Loss and Evolution of O-type Stars, ed. P. S. Conti, & C. W. H. de Loore (Dordrecht: D. Reidel Pub. Co.), IAU Symp., 83, 291
Oskinova, L. M., Ignace, R., Hamann, W.-R., Pollock, A. M. T., & Brown, J. C. 2003, A&A, 402, 755
Pallavicini, R., Golub, L., Rosner, R., et al. 1981, ApJ, 248, 279
Pittard, J. M., & Stevens, I. R. 2002, A&A, 388, L20
Pollock, A. M. T. 1987, ApJ, 320, 283
Pollock, A. M. T., & Corcoran, M. F. 2006, A&A, 445, 1093
Pollock, A. M. T., Haberl, F., & Corcoran, M. F. 1995, in Wolf-Rayet stars: binaries, colliding winds, evolution, ed. K. A. van der Hucht, & P. M. Williams (Dordrecht: Kluwer Academic Publ.), IAU Symp., 163, 512
Pollock, A. M. T., Corcoran, M. F., Stevens, I. R., & Williams, P. M. 2005, ApJ, 629, 482
Prilutskii, O. F., & Usov, V. V. 1976, Soviet Ast., 20, 2
Raassen, A. J. J., van der Hucht, K. A., Mewe, R., et al. 2003, A&A, 402, 653
Rauw, G. 1997, Contribution à l'étude de systèmes binaires massifs: détermination des paramètres fondamentaux et analyse des processus d'interaction dans des systèmes de type Of et WNL, Ph.D. Thesis, Université de Liège, Belgium
Rauw, G. 2006, in The X-ray Universe 2005, proceedings of the El Escorial conference, ESA SP-604, ed. A. Wilson (Noordwijck: ESA Publications Division), 1, 7
Rauw, G., Vreux, J. M., Gosset, E., Hutsemékers, D., & Magain, P. 1995, in Stellar Evolution: What Should Be Done?, ed. A. Noels, et al., Liège International Astrophysical Colloquium, 32, 463
Rauw, G., Vreux, J. M., Gosset, E., et al. 1996, A&A, 306, 771
Rauw, G., Vreux, J. M., Stevens, I. R., et al. 2002, A&A, 388, 552
Sana, H., Stevens, I. R., Gosset, E., Rauw, G., & Vreux, J. M. 2004, MNRAS, 350, 809
Sana, H., Rauw, G., Sung, H., Gosset, E., & Vreux, J. M. 2006, MNRAS, 372, 661
Schild, H., Güdel, M., Mewe, R., et al. 2004, A&A, 422, 177
Schweickhardt, J., Schmutz, W., Stahl, O., Szeifert, Th., & Wolf, B. 1999, A&A, 347, 127
Seward, F. D., & Chlebowski, T. 1982, ApJ, 256, 530
Seward, F. D., Forman, W. R., Giacconi, R., et al. 1979, ApJ, 234, L55
Skinner, S. L., Zhekov, S. A., Güdel, M., & Schmutz, W. 2002a, ApJ, 572, 477
Skinner, S. L., Zhekov, S. A., Güdel, M., & Schmutz, W. 2002b, ApJ, 579, 764
Skinner, S. L., Güdel, M., Schmutz, W., & Zhekov, S. A. 2006, Ap&SS, 304, 97
Smith, L. F. 1968, MNRAS, 138, 109
Stevens, I. R., Blondin, J. M., & Pollock, A. M. T. 1992, ApJ, 386, 265
Strüder, L., Briel, U., Dennerl, K., et al. 2001, A&A, 365, L18
Turner, M. J. L., Abbey, A., Arnaud, M., et al. 2001, A&A, 365, L27
Usov, V. V. 1992, ApJ, 389, 635
van der Hucht, K. A., Conti, P. S., Lundström, I., & Stenholm, B. 1981, Space Sci. Rev., 28, 227
Vink, J. S., de Koter, A., & Lamers, H. J. G. L. M. 2001, A&A, 369, 574
Waldron, W. L. 1984, ApJ, 282, 256
Wessolowski, U. 1996, MPE Rep., 263, 75
Willis, A. J., Schild, H., & Stevens, I. R. 1995, A&A, 298, 549
Zhekov, S. A., & Skinner, S. L. 2000, ApJ, 538, 808